Title: Temporal pattern separation in hippocampal neurons through multiplexed neural codes

Short Title: Neural codes supporting pattern separation in hippocampus

Authors: Antoine D. Madar[1], Laura A. Ewell[2], Mathew V. Jones[1]

Authors affiliations

[1]Department of Neuroscience, University of Wisconsin-Madison, USA

[2]Institute of Experimental Epileptology and Cognition Research, University of Bonn, Germany

Corresponding authors

Antoine D. Madar (madar@wisc.edu)

Author contributions

Conceptualization: MVJ, ADM. Data curation: ADM. Formal analysis: ADM, MVJ. Funding acquisition: MVJ, ADM. Investigation/data collection: ADM, LAE. Methodology: MVJ, ADM, LAE. Project administration: MVJ, ADM. Resources: N/A. Software: ADM, MVJ. Supervision: MVJ. Validation: MVJ, LAE, ADM. Visualization: ADM, MVJ. Writing – original draft: ADM. Writing – review & editing: MVJ, ADM, LAE.

Funding

This work was supported by the University of Wisconsin Institute for Clinical and Translational Research (M.V.J.; NIH/NCATS UL1TR000427) and Lily's Fund for Epilepsy Research (A.D.M.; 2015 fellow).

The authors declare no competing interests in relation to the present work.

Abstract:

Pattern separation is a central concept in current theories of episodic memory: this computation is thought to support our ability to avoid confusion between similar memories by transforming similar cortical input patterns of neural activity into dissimilar output patterns before their long-term storage in the hippocampus. Because there are many ways one can define patterns of neuronal activity and the similarity between them, pattern separation could in theory be achieved through multiple coding strategies. Using our recently developed assay that evaluates pattern separation in isolated tissue by controlling and recording the input and output spiketrains of single hippocampal neurons, we explored neural codes through which pattern separation is performed by systematic testing of different similarity metrics and various time resolutions. We discovered that granule cells, the projection neurons of the dentate gyrus, can exhibit both pattern separation and its opposite computation, pattern convergence, depending on the neural code considered and the statistical structure of the input patterns. Pattern separation is favored when inputs are highly similar, and is achieved through spike time reorganization at short timescales (< 100 ms) as well as through variations in firing rate and burstiness at longer timescales. These multiplexed forms of pattern separation are network phenomena, notably controlled by GABAergic inhibition, that involve many celltypes with input-output transformations that participate in pattern separation to different extent and with complementary neural codes: a rate code for dentate fast-spiking interneurons, a burstiness code for hilar mossy cells and a synchrony code at long timescales for CA3 pyramidal cells. Therefore, the isolated hippocampal circuit itself is capable of performing temporal pattern separation using multiplexed coding strategies that might be essential to optimally disambiguate multimodal mnemonic representations.

Introduction:

Understanding what computations hippocampal neurons perform and how they support episodic memory is a longstanding goal in neuroscience. The hippocampus is notably critical for the discrimination of memories that are similar in content (Kirwan et al., 2012). This cognitive function has long been hypothesized to be supported by a neural process called pattern separation, which is generally thought to be implemented in the dentate gyrus (DG) (Berron et al., 2016; O'Reilly & McClelland, 1994; Treves et al., 2008). Pattern separation is defined as the transformation of a non-simultaneous set of similar input patterns of neuronal activity into less similar output patterns (Santoro, 2013), and is theorized to happen in the hippocampus before encoding a memory trace in order to avoid confusion between similar memories (Rolls, 2010). Despite a long history of research on the subject, mostly in silico (Chavlis & Poirazi, 2017), it is still unclear how the activity of single neurons underlies this computation.

Generally speaking, single-neuron computations have been investigated experimentally using two broad strategies: 1) by determining how the spiking of individual neurons, recorded in vivo, is tuned to different parameters of the behavior or environment (Lisman et al., 2017) or 2) by relating the neuronal infra or suprathreshold membrane potential responses, generally recorded in vitro, to their synaptic inputs.

The first strategy has led to the discovery that the principal cells of the hippocampus fire preferentially in specific locations of an environment called place fields (O'Keefe, 1976). Upon sufficient modification of the environment, the place field(s) of a given neuron remap by relocating or changing their firing rate (in extreme cases, disappearing) (Colgin et al., 2008; Hainmueller & Bartos, 2018). These different forms of remapping have often been used as a proxy for pattern separation, yielding conflicting interpretations on the role of DG and CA3

(Leutgeb et al., 2007; Nakazawa, 2017; Neunuebel & Knierim, 2014). However, neurons remapping between two similar environments is not sufficient evidence that those neurons participate in pattern separation because place field remapping is assessed without knowledge of the direct synaptic inputs: it is possible that separated representations are inherited from upstream networks. Thus, despite extensive recordings of large populations of several hippocampal celltypes during behavior (Hainmueller & Bartos, 2018; Nakazawa, 2017), it remains unknown how each celltype participates in pattern separation.

In contrast to the first strategy, the second one explicitly takes into account the synaptic inputs of recorded neurons. Such an approach has been used to study dendritic integration (Krueppel et al., 2011), short (Hayakawa et al., 2015; Liu et al., 2014) or long-term plasticity (Bliss & Lomo, 1973; Lopez-Rojas et al., 2016) and the relationship between excitatory inputs and the output spiking probability (Dieni et al., 2016; Ewell & Jones, 2010; Lopez-Rojas et al., 2016; Mongiat et al., 2009; Pardi et al., 2015), but most of these studies were limited to simple input activity patterns (i.e. rhythmic series of spikes or bursts of spikes) and simple output patterns (i.e. a single spike). Some have used more complex sequences of spatially distributed synaptic inputs (Hyde & Strowbridge, 2012; Kamijo et al., 2014; Zylberberg et al., 2016), but the resulting input patterns were still spikes regularly spaced in time. Yet, neuronal spiketrains recorded in vivo are not so regular but instead approximately follow a Poisson distribution (Fellous et al., 2003) or a more bursty distribution (Legendy & Salcman, 1985; Weyand et al., 2001), and what neurons integrate is thus a barrage of irregular synaptic inputs (Destexhe et al., 2003; Pernía-Andrade & Jonas, 2014). To infer the single-neuron suprathreshold input-output relationship in more naturalistic regimes, some have thus recorded the spiking response to intracellular injections of current waveforms resulting from either white noise (Cook et al., 2007)

or from the simulated random discharges of a large number of presynaptic neurons (Destexhe et al., 2003; Fellous et al., 2003). But this only gives insight on the operations performed by a neuron isolated from its network. To understand the role of the network, rare studies have directly stimulated afferents with naturalistic spiketrains to characterize short-term (Dobrunz & Stevens, 1999; Fuhrmann et al., 2002; Gundlfinger et al., 2010) or long-term (Gundlfinger et al., 2010; Mistry et al., 2011) synaptic dynamics of hippocampal neurons. An even smaller number of studies have aimed at characterizing the suprathreshold input-output function of a neuron in response to external Poisson spiketrains (Berger et al., 1988a; Xie et al., 2006), and such experiments have determined that this function was different when evaluated with simpler input patterns (Berger et al., 1988b), confirming the necessity to assess neuronal computations with complex, naturalistic input patterns.

Surprisingly, because none of the above studies have quantified and systematically varied the similarity between input patterns, none have directly addressed how the input-output transformation in single hippocampal neurons relates to pattern separation. To answer this question, we stimulated, in mouse brain slices, afferent axons of the DG with complex input spiketrains of varying similarity and simultaneously recorded output spiketrains from a single neuron. Thus, in contrast to in vivo studies, we considered input and output temporal patterns instead of spatial ones. With this paradigm, we recently demonstrated that the suprathreshold responses of the principal neurons of the DG and CA3 were strongly decorrelated compared to their inputs, whereas DG interneurons exhibited less temporal decorrelation (Madar et al., 2018).

Importantly, our previous investigation only considered one type of neural code (binwise synchrony, as measured by the Pearson's correlation coefficient), even though temporal pattern separation could, in principle, be achieved in a variety of ways depending on the features

considered relevant in a spiketrain. For example, if the only feature carrying information in a spiketrain was its firing rate, a pattern separator would convert a series of input spiketrains with similar rates into a series of output spiketrains with dissimilar rates. Alternatively, the firing rate could be irrelevant and two output trains with the same number of spikes could be considered separated if their spiketimes are desynchronized. Pattern separation is thus a group of potential computations, each computation corresponding to a specific neural code, or, in other words, to a specific definition of "similarity". By testing a wide range of similarity metrics and timescales, the present work aims to determine through which neural codes temporal pattern separation is performed in the hippocampus.

Methods:

Herein, we revisit experiments performed in Madar et al. (2018) and expand on them by using additional types of input patterns, new pharmacological conditions, and by analyzing the previous and new datasets with multiple similarity metrics assuming different neural codes.

Experiments

All experiments were performed in accordance with the National Institute of Health guidelines outlined in the National Research Council Guide for the Care and Use of Laboratory Animal (2011) and regularly monitored and approved by the University of Wisconsin Institutional Animal Care and Use Committee.

Briefly, we performed experiments on C57Bl6 male mice (Harlan/Envigo) following the general paradigm described in Madar et al. (2018). Horizontal acute slices of a mouse brain hemisphere containing the hippocampus were prepared in cutting solution (CS; two version were

used. CS#1/CS#2, in mM: 83/80 NaCl, 26/24 $NaHCO_3$, 2.5/2.5 KCl, 1/1.25 $NaH2PO_4$, 0.5/0.5 $CaCl_2$, 3.3/4 MgCl2, 22/25 D-Glucose, 72/75 Sucrose, 0/1 Na-L-Ascorbate, 0/3 Na-Pyruvate, bubbled with 95% O_2 and 5% CO_2) and recorded in regular artificial cerebrospinal fluid (aCSF, in mM: 125 NaCl, 25 NaHCO3, 2.5 KCl, 1.25 NaH2PO4, 2 CaCl2, 1 MgCl2, and 25 D-Glucose). Two second input trains of varying similarity were delivered to neural afferents of DG or CA3 neurons via bipolar electrical stimulation through a glass theta pipette, while recording the membrane potential of a single responsive patched neuron in whole-cell current-clamp mode. For the intracellular solution (IS), we used two different recipes that yielded similar electrophysiological behaviors and results (IS#1/IS#2 in mM: 140/135 K-gluconate, 0/5 KCl, 10/0.1 EGTA, 10/10 HEPES, 20/20 Na-phosphocreatine, 2/2 Mg_2ATP, 0.3/0.3 NaGTP, 0/0.25 CaCl2, adjusted to pH 7.3 and 310 mOsm with KOH and H_2O). The location of the stimulation (>100um away from dendrites of the recorded neuron) and its intensity (0.1-1 mA) was determined to yield ~50% probability of spiking after an input pulse (range: ~20-80%). A stimulation protocol consisted of five or ten trains (i.e. a given input set), interleaved (with 5 s of pause between each train) and repeated ten or five times, respectively, such that fifty output traces were recorded (**Figure 1C**). The amount of pattern separation or convergence effectuated for a given recording was assessed by pairwise similarity analysis (defined below), displayed as what we refer to as a "pattern separation graph": the pairwise input similarity across all pairs of input trains (excluding self-comparisons) was compared to the average similarity of all pairs of output spiketrains coming from the corresponding pairs of input trains (excluding comparisons between output spiketrains coming from the same input train) (**Figure 1D-E**).

Figures 1-3 (GCs) and **Figures 8-9** (all celltypes) are based on recordings from GCs, fast-spiking interneurons (FSs), hilar mossy cells (HMCs) and CA3 pyramidal cells (CA3 PCs)

reanalyzed from Madar et al. (2018). They were performed on slices (CS#1 for GCs, CS#2 for other celltypes; IS#1 for all) from young mice (p15-25), using 11 input sets consisting of five Poisson spiketrains with a mean rate of 10 Hz (GCs, FSs, HMCs) or 30 Hz (CA3 PCs and their GC controls). Because it was very difficult to promote firing of CA3 PCs in aCSF, CA3 PCs and their GCs control were recorded in aCSF with 100 nM gabazine (gzn, SR-95531) to decrease inhibitory postsynaptic currents (IPSC) amplitude by 30% and allow CA3 PCs to occasionally escape inhibition and fire action potentials. Note that the GCs recorded in gabazine as controls for the CA3 PC experiments could not be directly compared to GC recordings in regular aCSF because input sets with different mean rates were used.

To determine the role of inhibition on pattern separation in GCs, we performed additional recordings of single GCs in slices from young mice (p22-32, 6 animals) (**Figure 7**). After cutting (CS#2), slices were moved to a storing chamber containing 100% CS, at 37°C for 30 minutes after dissection. As in all other experiments, the storing chamber was then placed at room temperature and slices left there for at least 30 min. Slices were then transferred to the recording chamber and perfused (5 ml/min) with oxygenated regular aCSF at 33-35°C. Patch-clamp recordings of GCs were performed using IS#1. An experiment consisted of recording the same GC under the same input set of five 10 Hz Poisson trains (average R_{input} = 0.76 at 10 ms, shown in **Figure 1B**) before and after addition of 100 nM gabazine to the flow of regular aCSF. We waited at least five minutes after the solution switch, to allow for equilibrium to be reached. The holding potential (~-70mV), the location of the stimulation electrode, the stimulus current intensity and all other parameters were unchanged between the two recordings (e.g. under gabazine, the spiking probability was not retargeted to ~50%, unlike the gabazine experiments using 30 Hz inputs mentioned above). The intrinsic properties of recorded GCs (n = 7) were

(mean ± SEM): 1) Before gzn: resting membrane potential V_{rest} = -76.5 ± 2.5 mV, input resistance R_i = 194 ± 30 MΩ and membrane capacitance C_m = 20 ± 1.4 pF; 2) After gzn: V_{rest} = -74.4 ± 2 mV, R_i = 184 ± 29 MΩ and C_m = 17 ± 1.6 pF. R_i was not significantly affected and V_{rest} and C_m were only slightly decreased after treatment (Wilcoxon signed rank test: V_{rest} p = 0.09; R_i p = 0.44; C_m p = 0.03). The slight drift of C_m was likely due to the small increase in access resistance occurring over time (before: 6 ± 0.8 MΩ, after: 7.3 ± 1.4 MΩ; p = 0.06).

To explore the impact of a variety of input pattern statistical structures on single neuron computations, we designed two new input sets comprised of 10 different two seconds spiketrains (**Figure 4-6**). Trains in "input set A" follow a Poisson (P) distribution and have an average Pearson's correlation of 75% at the 10 ms timescale, but each train has a different mean firing rate (P ΔFR, **Figure 4A**). Trains in "input set B" do not follow a Poisson distribution: they all have 21 spikes, making them all 10.5 Hz overall, but are more or less bursty (B) (i.e. for each spiketrain the same number of spikes was distributed in a different number of time bins. Occupied time bins were selected randomly – following a uniform distribution – among all the possible time bins) (B 10.5 Hz, **Figure 4B**). For these experiments, we used slices from two adult mice (p145 and p153) injected with saline at p46 as controls for a separate set of experiments (not described here). Slices were prepared as described above (CS#2) and patch-clamp recordings were performed in regular aCSF using IS#2. The intrinsic properties of recorded GCs were: 1) Input set A (n = 5): V_{rest} = -80.4 ± 2.9 mV, R_i = 155 ± 19 MΩ and C_m = 23 ± 2 pF; 2) Input set B (n = 3): V_{rest} = -78.0 ± 5.5 mV, R_i = 178 ± 14 MΩ and C_m = 24 ± 3 pF.

All chemicals and drugs were purchased from Sigma-Aldrich (USA).

Similarity metrics

We assessed the similarity between spiketrains in four ways, spanning a range of different assumptions on the neural code: 1) with the Pearson's correlation coefficient (R), 2) with the normalized dot product (NDP), 3) with the scaling factor (SF) and 4) with a distance metric called SPIKE specifically designed to assess the dissimilarity between two spiketrains (Kreuz et al., 2013). In addition, we used measures of differences between spiketrains that assume different neural codes, related to the one assumed by SF but easier to interpret in terms of basic spiketrain features (see **Firing rate and burstiness codes** and **Dispersion metrics** sections below).

For R, NDP and SF, two spiketrains X and Y of the same duration were divided into N time bins of duration τ_w, with X_i and Y_i the respective numbers of spikes in bin i for each spiketrain. In contrast, the SPIKE metric is binless and based on the spike times of each spiketrain. For all similarity measures, empty spiketrains (i.e. sweeps during which no spikes were evoked) were excluded.

R can take values between 1 (perfectly correlated) and -1 (anticorrelated) with 0 indicating X and Y are uncorrelated, i.e. dissimilar. It was computed with the following equation, where *cov* is the covariance (scalar), σ is the standard deviation and $\bar{X}$ and $\bar{Y}$ are the means of X and Y:

$$R = \frac{cov(X,Y)}{\sigma_X . \sigma_Y} = \frac{\sum_{i=1}^{N}(X_i - \bar{X})(Y_i - \bar{Y})}{\sqrt{\sum_{i=1}^{N}(X_i - \bar{X})^2}\sqrt{\sum_{i=1}^{N}(Y_i - \bar{Y})^2}} \qquad (eq\ 1)$$

NDP is the cosine of the angle θ between the two vectors: it is 0 when they are perfectly orthogonal, 1 when they are collinear (see **Figure 2A, C**). NDP was computed as the scalar

product of X and Y divided by the product of their norms, with the following equation (where X_i and Y_i are the coordinates of X and Y):

$$\mathrm{NDP} = \cos(\theta) = \frac{\sum_{i=1}^{N} X_i Y_i}{\sqrt{\sum_{i=1}^{N} X_i^2}\sqrt{\sum_{i=1}^{N} Y_i^2}} \qquad (eq\ 2)$$

SF quantifies the difference of length between the two vectors X and Y. We have defined it as the ratio between the norms of each vector, the smaller norm always divided by the bigger one to have SF values ranging from 0 to 1. SF = 1 means X and Y are identical in terms of binwise spike number. The closer to 0 SF is, the more dissimilar are X and Y (see **Figure 2A, C**). SF was computed with the following equation (where $0 < ||X|| \leq ||Y||$):

$$SF = \frac{||X||}{||Y||} = \frac{\sqrt{\sum_{i=1}^{N} X_i^2}}{\sqrt{\sum_{i=1}^{N} Y_i^2}} \qquad (eq\ 3)$$

NDP and SF focus on complementary features of a system of two vectors (angle vs norms), and thus, together they are sufficient to fully describe the similarity between two vectors in a Euclidean space.

The binless SPIKE similarity metric was computed from lists of spike times using the Matlab toolbox provided at **www.fi.isc.cnr.it/users/thomas.kreuz/sourcecode.html**. The provided software computes the SPIKE-distance between two spiketrains (called D(t) in our study and S(t) in eqn. 19 of the original paper) (Kreuz et al., 2013) and we derived the SPIKE similarity as:

SPIKE = $1 - \frac{1}{T}\int_0^T D(t)dt$, where T is the duration of the spiketrain. Because D(t) ranges from 0 to 1, SPIKE is thus also between 0 and 1, like NDP and SF. When SPIKE is equal to 1, spiketrains have exactly the same spike times, i.e. they are synchronous (n.b. in our experiments, spiketrains were not simultaneously recorded, but we use "synchronous" in the sense of spiketrains aligned to the start of each sweep). Note that SPIKE has a large dynamic range (i.e. sensitivity over large differences of spiketimes), and, as a result, realistic spiketrains like in our input sets rarely have a SPIKE similarity lower than 0.5 (Kreuz et al., 2013) (see **Figure 3D**).

The ranges of possible values for the metrics we used are listed below, where closer to 1 always means more similar:

$-1 \leq R \leq 1$
$0 \leq NDP \leq 1$
$0 < SF \leq 1$
$0 \leq$ SPIKE-similarity ≤ 1; but ≥ 0.5 in most cases

Each metric assumes a specific neural code. For instance, R, NDP and SF all consider that the basic informative feature in spiketrains is the number of spikes in a time bin (i.e. a spikecount code), but R and NDP suppose that spiketrains are similar when the spikecounts increase or decrease similarly in the same time bins (with empty bins not counting for NDP), thus assuming a binwise synchrony code, whereas SF assumes a code where it is the similarity in overall burstiness or firing rate that is relevant (see **Figure 4A-B**), not the binwise synchrony (see **Figure 2A-C**). SPIKE, on the other hand, considers a spike time synchrony code. Details on the neural codes assumed by each metric, how they differ from each other and how they are

impacted by global increases in firing rate can be found in the **Supplements** (part 1). The main assumptions and properties of each similarity metric on the neural code are summarized in **Table S1**.

Firing rate and burstiness codes

R, NDP, SF and SPIKE are considering different aspects of spiketrains and thus assume different neural codes. However, it can be difficult to interpret those similarity measures in terms of common properties of spiketrains like the firing rate or the burstiness. To get a better sense of the neural code assumed by each similarity metric, and to directly assess whether pattern separation was performed through easily interpretable strategies like variation of the firing rate or variation of the burstiness, we measured such properties in each spiketrain.

The firing rate is simply the number of spikes divided by the duration of a sweep (2 seconds). Measuring burstiness is less straightforward as there is currently no consensus on the definition of a burst of action potentials (Cotterill et al., 2016; Lobb, 2014; Robin et al., 2009). We used three measures, detailed below.

Spiketrains are often considered bursty when it diverges from a Poisson process (Cotterill et al., 2016; Legendy & Salcman, 1985). To determine the tendency of a neuron to fire bursts, we computed the burstiness of a given output set as the Kullback-Leibler divergence (D_{KL}) of its interspike interval (ISI) frequency distribution M (normalized to the median ISI) from the normalized ISI frequency distribution P of a Poisson process. In practice, output sets from a 10 Hz input set were compared to the ISI distribution from all combined 10 Hz input sets, whereas input sets from 30 Hz input set were compared to the combined distribution of all 30 Hz input sets.

$$Burstiness = D_{KL}(M||P) = \sum_j M(j) \log\left(\frac{M(j)}{P(j)}\right) \qquad (eq\ 4)$$

where M(j) or P(j) is the value of M or P in the jth bin of the distribution. Normalized ISI frequency distributions were discretized in 250 bins going from 0 to 50. See **Supplements** (part 2) for details on why D_{KL} is a suitable measure of cell burstiness.

To assess burstiness in single spiketrains, the D_{KL} measure being not well-suited for this (see **Supplements - 2**), we designed two simple nonparametric measures that we called *compactness* and *occupancy*. Instead of explicitly defining "burstiness", these measures are based on the binning of spiketrains, offering the advantage of being directly comparable to the neural codes assumed by binned similarity metrics like R, NDP and SF (**Figure S2**). A spiketrain is thus seen as a vector of spikecounts, and a time bin (or vector coordinate) is considered a window in which spikes can be clustered. Thus, instead of counting the number of detected bursts and the number of spikes in a burst, our two measures provide information on the number of occupied bins (Compactness) and the number of spikes in occupied bins (Occupancy). These measures of burstiness should be viewed as complementary to previous definitions, not as replacements.

The compactness of a spiketrain was computed as follows:

$$\begin{aligned} Compactness &= 1 - proportion\ of\ occupied\ bins \\ &= 1 - \frac{number\ of\ bins\ with\ at\ least\ 1\ spike}{total\ number\ of\ bins} \qquad (eq\ 5) \end{aligned}$$

Compactness thus runs between 0 (all bins are occupied by at least one spike) and 1 (no spikes: this case was excluded so the true maximum, corresponding to any spiketrain with all its spikes clustered in just one bin, was $1 - \frac{1}{total\ number\ of\ bins}$). Values closer to 1 mean very few bins are occupied: either many spikes are clustered in a small number of bins or the measured spiketrain has very few spikes.

The occupancy of a spiketrain is the average number of spikes per occupied bin:

$$Occupancy = \frac{number\ of\ spikes}{number\ of\ occupied\ bins} \qquad (eq\ 6)$$

Because we excluded empty spiketrains, the occupancy can theoretically go from 1 to infinity. Note that the lowest value (i.e. 1 spike per occupied bin) means that all spikes are distributed in different bins (or that there is just 1 spike).

Compactness and occupancy are both dependent on the firing rate of a given spiketrain, but not in the same way (see **Supplements - 2** for details). They are complementary measures that, together, allow determining whether two spiketrains with different firing rates are also different in terms of burstiness (**Table S2**). When spiketrains have the same firing rate (e.g. input set B 10.5 Hz in **Figure 4B**, which were all spiketrains with 20 spikes each but were constructed by specifying different numbers of occupied bins), compactness and occupancy are redundant (**Figure S2C-D**) and, for both measures, higher values mean higher burstiness.

Dispersion metrics

To assess the amount of pattern separation performed by variation of a given spiketrain feature like the firing rate, compactness or occupancy, we measured the difference in this feature

between two spiketrains. In the same spirit as for similarity metrics, we could then compute the difference between all pairs of trains in an input set (excluding self-comparisons) and compare to the difference of all corresponding pairs of output spiketrains, (excluding comparisons between output spiketrains associated with the same input spiketrain). This would yield matrices of pairwise differences organized in the same fashion as the similarity matrix displayed in **Figure 1E**, which could then be converted to pattern separation graphs showing the average pairwise output absolute difference as a function of the pairwise input difference (**Figure 6A**). Note that the mean absolute difference (MAD) between all spiketrains of a given set (either input or output) corresponds to the Gini mean difference (Yitzhaki, 2003), a common measure of dispersion of a sample akin to the standard deviation (**Figure 5A**). The difference in MAD between an input set and its output set indicates whether pattern separation or convergence was achieved through variation of the measured spiketrain feature (**Figure 6B**).

Software and statistics

Data analysis was performed using MATLAB (Mathworks, Natick, MA, USA). Sample sizes were chosen based on the literature and estimations of the variance and effect size from preliminary data. The one-sample Kolmogorov-Smirnov test was used to verify the normality of data distributions. Parametric or non-parametric statistical tests were appropriately used to assess significance (p-value < 0.05). Assumptions on equal variances between groups were avoided when necessary. All tests on means or medians were two-tailed. To determine whether distributions of similarity values [S_{input}, S_{output}] (S standing for any similarity metric) were significantly different (**Figure 7, 8**), we performed an analysis of the covariance (ANCOVA) using separate lines regression models (the *aoctool* function and a custom-written code yielded

the same results). The 95% confidence interval around the slope and intercept of a given linear model was determined from the *regress* function (**Figure 8**).

Results:

Temporal pattern separation via decorrelation, orthogonalization and scaling

In Madar et al. (2018), we demonstrated for the first time that single GCs exhibit high levels of pattern decorrelation thanks to a novel pattern separation assay in acute brain slices. Our general paradigm has three steps (**Figure 1**): 1) ensembles of stimulus patterns (simulating trains of action potentials) are generated, with known degrees of similarity to each other. These sets of input spiketrains are then fed into the DG by stimulating the lateral perforant path. 2) The simultaneous response of a single neuron is recorded in whole-cell current-clamp. 3) The similarity between the output spiketrains is compared to the similarity between the input patterns, revealing the degree of separation or convergence.

We first reanalyzed a dataset, presented in Madar et al. (2018), of GC recordings performed in response to input sets constituted of 10 Hz Poisson trains (**Figure 1B**). A pairwise similarity analysis (**Figure 1E**), with the Pearson's correlation coefficient R as a measure of similarity, confirmed our finding that the output spiketrains of GCs are significantly less correlated than their inputs at both low and high input correlations (**Figure 1F**). As detailed in Madar et al. (2018), even the repetition of the same input train leads to decorrelated output trains, due to the probabilistic nature of synaptic transmission.

We used R as a similarity measure between spiketrains, because it is easy to implement and is commonly used to quantify the similarity between neural activity patterns, both in

computational (Yim et al., 2014) and experimental studies (Danielson et al., 2017; Leutgeb et al., 2007; Neunuebel & Knierim, 2014; Senzai & Buzsáki, 2017). However, the original Hebb-Marr framework theorized pattern separation as the orthogonalization of the input patterns (Hopfield, 1982; McNaughton & Morris, 1987; Santoro, 2013). As a result, the terms "decorrelation" (corresponding to output patterns, viewed as variables, with a lower Pearson's correlation coefficient than their inputs) and "orthogonalization" (corresponding to output patterns, viewed as vectors, that are closer to a right angle than inputs) are often conflated in the literature, even though they are not mathematically equivalent and have a nonlinear relationship to each other (**Figure 2A-C, S1**. See **Methods – Similarity metrics** and **Supplements - 1**). For instance, pairs of spiketrains can be uncorrelated (R = 0) without being orthogonal, or can be orthogonal without being uncorrelated (**Figure 2A-C** and **S1**). To determine whether output spiketrains of GCs are truly orthogonalized, we explicitly considered spiketrains as vectors and computed the normalized dot product (NDP) between pairs of spiketrains to assess their similarity (**Figure 2A, C**. See **Methods – Similarity metrics** and **Supplements - 1**). For every recording set, NDP_{output} was lower than NDP_{input}, indicating that the angle between output spiketrains was closer to a right angle (i.e., closer to orthogonal) than their inputs (**Figure 2D-E**).

Vectors can differ by their angle, but also by their norm. In other words, even if neurons fire in the same time bins (relative to the start of each sweep), the number of spikes per bin can be different, as quantified by the ratio between their norms (scaling factor, SF) (**Figure 2A, C.** See **Methods – Similarity metrics** and **Supplements - 1**). Our results show that for input patterns highly similar in terms of SF, SF_{output} is slightly but significantly lower than SF_{input} (**Figure 2F**). This indicates that variations in the binwise firing rate of single GCs in response to similar inputs is a potential, but weak, mechanism of pattern separation at the 10 ms timescale.

As a whole, these results confirm that input spiketrains are decorrelated in the DG at the level of single GCs, and demonstrate that, at the 10 ms timescale, GCs exhibit temporal pattern separation mediated by high levels of orthogonalization and weak levels of scaling.

Pattern separation of spiketrains occurs through multiplexed neural codes

Trains of action potentials can be described in many different ways: their overall firing rate, the timing of their spikes or the number of bursts of spikes, among other statistics (from now on referred to as *spiketrain features*). Measuring the similarity between two spiketrains is not a trivial problem, if only because it is unclear what spiketrain features are relevant to the brain and what counts as different or similar. In principle, pattern separation could be achieved by the variation of any spiketrain feature (e.g. if the relevant feature is the total number of spikes in two second bins, pattern separation will be achieved if this number varies more in the set of output spiketrains than in the input set). In other words, many different forms of pattern separation could be performed depending on the neural code considered. In our analyses, the neural code (i.e. the set of assumptions on which spiketrain features are considered relevant and what definition of similarity is used) is determined by the choice of similarity metric and time resolution (see **Supplements – 1**). In order to better characterize which neural code(s) are used to perform temporal pattern separation in the hippocampus, we thus tested multiple metrics and timescales. This approach also allowed us to ask whether several coding strategies could be multiplexed (i.e. simultaneously relevant over different timescales) to achieve pattern separation.

The three measures of similarity we have used above (R, NDP and SF) all carry different assumptions about the neural code (**Table S1)**: R and NDP are mostly, but differently, sensitive to the binwise synchrony whereas SF evaluates the local variations in spike number (**Figure 2A-**

C and see **Supplements - 1**). On the other hand, these metrics resemble each other in that they require binning spiketrains in time windows of a prespecified duration (τ_w). The timescales that are meaningful for the brain are uncertain so we assessed the separation of spiketrains for different τ_w. Indeed, different durations of τ_w assume a different window to read the information contained in a spiketrain. Our analysis shows that pattern separation, measured through R or NDP, is more pronounced at short timescales (e.g. 5 ms) than at longer ones (e.g. 100 ms) (**Figure 3A-B**). In contrast, in the case of high input similarity, pattern separation through scaling is rather weak at short timescales but gets stronger at longer ones (**Figure 3C**). This demonstrates that multiplexed coding allows temporal pattern separation to be carried out by the DG for a large range of timescales.

In addition, because a long stream of research suggests that spiketrains can carry information directly through the timing of individual spikes (Gutig, 2014; Rieke et al., 1999; VanRullen et al., 2005), we also assessed the similarity between spiketrains using SPIKE, a binless metric purely based on spike times (Kreuz et al., 2013), thus assuming a neural code completely different from the binned metrics above (**Methods – Similarity metrics** and **Supplements**, **Table S1**). Our results show that input spiketrains with similar spike times relative to their sweep start (defined here as spiketrains with a high degree of *synchrony*, see **Methods – Similarity metrics**), are transformed into significantly less synchronous outputs, thereby demonstrating that temporal pattern separation in single GCs can occur through spike timing modifications (**Figure 3D**). This is consistent with the high levels of decorrelation and orthogonalization at very short timescales (**Figure 3A-B**) and confirms that temporal pattern separation can be achieved through multiple coding strategies.

Single GC computations depend on the statistical structure of their input patterns

Results in **Figure 2F** and **3C** show that the similarity of GCs output spiketrains in terms of SF is almost flat, suggesting it might be independent of the input similarity, hence leading to significant pattern convergence in certain conditions of low input similarity and short timescales. However, those experiments were based on responses to ~10 Hz Poisson input spiketrains that did not differ much in terms of SF. To further characterize single GC computations, we designed two new input sets spanning a wider range of SF values (**Figure 4A-B**). From its definition, it was apparent that, unlike R and NDP, SF is very sensitive to both differences of overall firing rate and differences in burstiness between spiketrains (**Figure S2**). Input set A was thus made of highly correlated Poisson spiketrains with different firing rates (7-31.5 Hz), and input set B was made of uncorrelated spiketrains with constant firing rate but different levels of burstiness (see **Methods - Experiments**). By recording the spiking output of single GCs in response to these input sets we could thus test how GCs transform input patterns with vastly different statistical structures, and whether they can still perform pattern separation in those conditions. Our results indicate that for both input sets GCs can perform weak levels of pattern separation via scaling for highly similar inputs (**Figure 4C**), consistent with our experiments using 10 Hz Poisson trains (see Figure 2F and 3C). However, although not independent of input similarity, the similarity of GCs output spiketrains (in terms of SF) is comprised in a relatively narrow band, yielding high levels of pattern convergence for relatively dissimilar input spiketrains (**Figure 4C**). In other words, when assuming a neural code based on the norm of spikecount vectors, GCs outputs are maintained relatively similar to each other, even when their corresponding input patterns are very different. This is true from the millisecond to the second timescale, but pattern convergence

decreases and separation increases with longer timescales (**Figure 4C**), consistent with previous experiments (see Figure 3C).

Although SF makes mathematical sense when measuring the similarity between vectors, it is difficult to interpret in terms of basic spiketrain features, in part because it is sensitive to both firing rate and burstiness (see **Supplements – 1** for details). We thus aimed to gain a more intuitive view of how those spiketrain features vary to result in pattern separation or convergence. For that, we calculated the mean firing rate of each spiketrain and designed two new indicators providing complementary information on the burstiness of individual spiketrains: compactness and occupancy (**Figure 5A**). Briefly, compactness is anticorrelated to the number of time bins occupied by at least one spike (the less occupied bins, the more compact a spiketrain is), whereas occupancy is the average number of spikes per occupied bin (**Methods – Firing rate and burstiness codes** and **Supplements - 2**).

First, we asked how GCs transform their inputs in terms of firing rate and burstiness. For all timescales, GCs have generally equal or higher compactness than their inputs but maintain a constant low range of occupancy (**Figure 5B left**). This combination suggests that, using **Table S2**, GC responses are mostly a sparser version of their inputs, with a decrease in intra-burst frequency when inputs are bursty. Accordingly, the overall firing rate of GC output spiketrains is generally maintained lower than their inputs (**Figure 5B right**), which is consistent with the known sparsity of GC activity in vivo and fits the view of the DG acting as a filter of cortical activity (Dengler & Coulter, 2016).

We next asked whether temporal pattern separation is performed through variation of the firing rate between GCs output spiketrains, or through variations of compactness or occupancy, or a combination of those three. Our results indicate that pattern separation, but also pattern

convergence, can be exhibited for all three types of codes, depending on certain conditions (**Figure 6**). First, separation is favored at longer timescales (for burstiness codes) and high input similarity (for burstiness and rate codes) (**Figure 6A**). Second, the direction of the computation (separation or convergence) strongly depends on the statistical structure of the input patterns (**Figure 6B**): 1) In response to Poisson inputs with very similar firing rates (P 10 Hz), GCs exhibit low but significant levels of pattern separation through small variations of compactness, occupancy and firing rate, which become more relevant with larger timescales. Pattern separation measured through scaling (see Figure 2F and 3C) was thus due to the variability in all three spiketrain features combined. 2) In response to Poisson inputs with varying firing rates (P ΔFR, input set A), GCs, as the timescale is increased, switch from pattern convergence to pattern separation through compactness variations, while increasing their levels of convergence in terms of occupancy. Accordingly, their output spiketrains have more similar firing rates than their inputs (this is because GCs maintain a narrow range of firing rates regardless of the rate of their inputs, as shown in Figure 5B). 3) In response to inputs with a constant firing rate but varying levels of burstiness (B 10.5 Hz, input set B), GCs show low but significant pattern convergence in terms of compactness, larger levels of pattern convergence in terms of occupancy that progressively switch to pattern separation at the largest timescale (≥1s), which translates into significant pattern separation through variations of the firing rate (which is equivalent to an occupancy code at the 2s timescale). Interestingly, this analysis demonstrates that GCs can exhibit both separation and convergence simultaneously through different neural codes: for instance, at the 250 ms timescale, the compactness of GCs output spiketrains vary more than the compactness in input set A, whereas GCs output spiketrains occupancy vary less (**Figure 6B, Table 1**).

Inhibition enforces temporal pattern separation in GCs.

GCs are known to receive strong feedforward and feedback inhibition from a variety of GABAergic interneurons (Hosp et al., 2014; Ramaswamy, 2015) that impact GCs spiking output (Ewell & Jones, 2010; Hsu et al., 2016; Lee et al., 2016). Furthermore, theoretical work has long suggested a role for interneuron interactions with GCs in mediating pattern separation (Myers & Scharfman, 2009; O'Reilly & McClelland, 1994; Temprana et al., 2015), but experimental evidence is lacking. To test the influence of fast inhibitory transmission on the complex computations of GCs characterized above, we recorded GCs responses to 10 Hz Poisson trains before and after application of a nonsaturating concentration of Gabazine, a $GABA_A$ receptor antagonist (**Figure 7A**, see **Methods - Experiments**). Under these conditions, IPSC amplitude was reduced by ~30% (not shown), which led to a slight but visible increase in firing rate, in part due to a higher propensity to fire short bursts of action potentials riding a single EPSP (**Figure 7A-B**). This pharmacological manipulation led to lower levels of temporal pattern separation as measured by R, NDP, but also SF (**Figure 7C**). This was true at all timescales (**Figure 7D**), with the importance of inhibition for pattern separation even increasing at longer timescales. Interestingly, the impact on pattern separation at larger timescale was not only for SF, whose relevance increases with larger τ_w (see Figure 3C) but also for R and NDP, whose relevance normally decreases with larger τ_w (see Figure 3A-B).

The average R_{output} was well correlated to the average firing rate of a recording set (linear regression: $R^2 = 94\%$, $p < 0.0001$, n = 14 data points from 7 GCs), suggesting that the inhibitory control of sparsity in GCs firing helps temporal pattern separation as measured with R. Interestingly, in a previous report we did not detect such a strong relationship between R and the

firing rate levels of GCs (Madar et al., 2018). Moreover, R is mathematically independent of proportional increases of pairwise firing rate levels and not very sensitive to non-proportional ones (see **Supplements - 1** and **Figure S1C**). In the present experiment, the correlation between R and the firing rate is thus likely to arise from physiological reasons that conjointly affect both the sparsity and the binwise synchrony of output spiketrains rather than from the mathematical assumptions behind R.

In contrast to R and NDP, the mathematical definition of SF makes it sensitive to pairwise firing rate levels (i.e. SF systematically increases for pairs of spiketrains with higher firing rates. See **Supplements - 1** and **Figure S1C**). As seen before, SF is also designed to be sensitive to differences in firing rate and burstiness of individual spiketrains (e.g. Figure 5 and S2). Therefore, the effect of gabazine on decreasing pattern separation as measured by SF (**Figure 7C-D**) could be due: 1) to a global increase in firing rates in all the output spiketrains, 2) to variations of firing rate or burstiness between output spiketrains, or 3) to a combination of all of the above. The direct assessment of pattern separation in terms of firing rate or burstiness indicates that inhibition actually doesn't affect temporal pattern separation through rate or compactness codes and favors pattern convergence through occupancy codes (**Figure 7E**). We can thus conclude that the effect of inhibition on pattern separation via scaling (SF) is mostly due to the global firing rate increase under gabazine.

Overall, we provide here the first experimental evidence that fast inhibitory transmission in the DG controls levels of temporal pattern separation and convergence through different multiplexed neural codes.

Different hippocampal celltypes support pattern separation through different neural codes

GCs are embedded in a network of multiple celltypes all participating in generating the output of the DG. For instance, computational models of the DG have suggested that different populations of inhibitory and excitatory interneurons could modulate certain forms of pattern separation (Danielson et al., 2017; Myers & Scharfman, 2009). To develop a comprehensive understanding of the computations performed by the DG, and hippocampal networks in general, it is important to characterize the input-output transformation of a diverse set of celltypes. We recorded from dentate fast-spiking GABAergic interneurons (FSs), glutamatergic hilar mossy cells (HMCs) and CA3 pyramidal cells (PCs) in response to 10 Hz (for GC, FS, HMC) or 30 Hz (for PC and GC) Poisson input trains with varying levels of correlation (**Figure 8A** and **Methods – Experiments**).

Previously, we found that temporal pattern separation, measured using R, was not specific to GCs but that GCs exhibit the highest levels of decorrelation among tested dentate neurons, and that CA3 PCs express even more temporal decorrelation than GCs (Madar et al., 2018). Here we ask whether this is still the case when considering other neural codes based on different similarity metrics. A pairwise similarity analysis and a comparison of the pattern separation function (the linear regression model describing S_{output} as a function of S_{input}, with S representing a given similarity metric) across celltypes shows that pattern orthogonalization (NDP) and scaling (SF) levels significantly differ at most timescales (**Figure 8B-C**).

For NDP, we notice a progression from FSs to HMCs to GCs to CA3 PCs, with GCs performing the highest levels of separation among DG neurons, and CA3 PCs surpassing GCs, especially with their ability to orthogonalize inputs already relatively dissimilar (**Figure 8B**). The orthogonalization function of GCs, HMCs and CA3 PCs diverge as the timescale is increased (**Figure 8C**).

For SF, scaling functions do not depend much on the input similarity, except for CA3 PCs. Mostly based on the scaling functions intercept, we notice two groups (**Figure 8B-C**): FSs and GCs exhibit low levels of pattern separation through scaling, in contrast to HMCs and CA3 PCs (and their GC controls) that produce spiketrains with lower similarities in terms of SF. Note that among celltypes tested with 10 Hz Poisson trains, HMCs are the best at pattern separation through scaling, not GCs.

In contrast to GCs, HMCs and FSs tend to fire bursts of spikes (although the characteristics of bursts differ between the two celltypes), which affects, at least partially, their levels of pattern decorrelation (Madar et al., 2018). An analysis of the distribution of interspike-intervals in all recorded celltypes confirmed that HMCs and FSs are bursty but not in the same way (**Figure 9A**). It also revealed that, although neither CA3 PCs nor their GC controls (recorded under gabazine and 30 Hz inputs) displayed bursts elicited by a single input pulse (Madar et al., 2018), they can be considered bursty in the sense that their output spikes tend to be clustered together in time in a nonrandom fashion (**Figure 9A**). We thus asked whether these celltypes with diverse bursty behaviors could perform pattern separation through compactness, occupancy or firing rate codes. Our analysis shows indeed that these features vary across the output spiketrains of hippocampal neurons, but in different ways for each celltype: at all timescales, FSs and HMCs achieve more pattern separation through variations of occupancy and firing rate, whereas CA3 PCs achieve more pattern separation through variations of compactness (**Figure 9B, Table 2**).

Overall, we demonstrate here that not all hippocampal celltypes exhibit the same computations, but that they all can perform temporal pattern separation to different degrees through different neural codes and over different timescales. This suggests that different types of

neurons can serve different, complementary, computations that allow the isolated hippocampal network to perform temporal pattern separation using multiplexed coding strategies.

Discussion

In summary, we report that the hippocampus can perform temporal pattern separation or convergence at the level of single neurons through different multiplexed neural codes. Pattern separation can be achieved by varying many different spiketrain features in the ensemble of output spiketrains, like the spike times, the firing rate, the number of bursts or the number of spikes in a burst. We found that GCs, the output neurons of the DG, mostly use a "desynchronization" strategy leading to an orthogonalization of their output spiketrains, especially at short timescales. When considering a neural code focused on firing rates or burstiness, GC output varies little, leading to pattern convergence or separation depending on the degree of similarity of the inputs. Other hippocampal neurons perform different computations through complementary combinations of various neural codes (mostly rate for FSs, burstiness for HMCs and synchrony at long timescales for CA3 PCs), and their network interactions constrain the ability of the hippocampus to perform temporal pattern separation, notably through inhibition of GC activity. Given that, during behavior, hippocampal neurons have a mixed selectivity to different aspects of the environment and cognitive tasks contingencies (Eichenbaum, 2017; Lin et al., 2005; McKenzie et al., 2014), the use of multiplexed codes is likely critical to encode rich representations efficiently (Panzeri et al., 2010). Therefore, the multiplexed forms of pattern separation we have characterized here might be essential to optimally disambiguate between similar multidimensional memories.

The hippocampus performs multiplexed forms of pattern separation

Overall, our study highlights that measuring neuronal computations implies a certain vision of the neural code, and that brain networks or single neurons perform many different computations depending on the assumed coding scheme.

The "neural code" is a pervasive but vague concept that refers to the set of features of neural activity that convey information, for example to represent our experiences and memories. The first difficulty in breaking this code comes from the infinitely large number of potential features and combinations of features that could be relevant in the brain. Since the early work of Adrian (Adrian, 1928), the most common view is that neurons transmit information about their stimulus through their firing rate, i.e. the number of output spikes averaged over a certain time window. This rate code is often contrasted to time codes, but this is a false dichotomy (Rieke et al., 1999): there is an infinite number of possible rate codes, as there is an infinite number of time windows over which the number of spikes could be integrated (are spikes counted by reader neurons over milliseconds, seconds or minutes?). In addition to spikecounts, information can also be carried by the timing of single spikes (Osborne et al., 2008; Rieke et al., 1999; VanRullen et al., 2005), bursts (Kepecs & Lisman, 2003; Mease et al., 2017) or even more complex spike patterns (Dettner et al., 2016; Lundstrom & Fairhall, 2006; Oram et al., 1999; Osborne et al., 2008). Even when focusing on time or burstiness codes, many subfeatures could be considered words in the elusive language of the brain: for example, the information could be encoded in the specific spike times (Thorpe et al., 2001) or the interspike intervals (Chacron et al., 2001; Lundstrom & Fairhall, 2006), the relative or exact latency or synchrony with regard to other spiketrains (Thorpe et al., 2001) or the relative timing of individual spikes with regard to a reference network oscillation (Lisman & Jensen, 2013), the timing or frequency of bursts

(Kepecs & Lisman, 2003; Mease et al., 2017), the spike times within a burst or the spikecounts per burst (Elijah et al., 2015; Mease et al., 2017).

Pattern separation has long been thought to cover several potential computations depending on the neural code considered (Santoro, 2013). Indeed, past investigations did not always define brain activity patterns the same way, nor did they choose the same similarity metrics and time resolution, thus assuming different forms of pattern separation. When the hypothesis of pattern separation was first formulated, activity patterns were defined as binary vectors representing populations of ON or OFF neurons, without considering a time dimension (McNaughton & Morris, 1987; O'Reilly & McClelland, 1994; Rolls, 2010). As a result, modeling work that followed often excluded the dynamics of neural activity, and used the number of common active neurons between two population patterns as their measure of similarity (Chavlis et al., 2017; Danielson et al., 2017; Myers & Scharfman, 2009). In addition to this purely spatial population code, others have defined activity patterns as maps of firing rates averaged over minutes, or as population matrices of those maps (Leutgeb et al., 2007; Nakazawa, 2017), measuring pattern separation using R (Neher et al., 2015) or NDP (Aimone et al., 2009) as their similarity metric. Only two modeling studies have investigated pattern separation by directly considering spiketrains at a timescale less than a minute: one considered an input pattern as a static population of ON/OFF neurons, an output pattern as a population vector of firing rates averaged over 500 ms and the similarity between two output patterns was based on the sum of firing rate ratios (Chavlis et al., 2017); the second considered an input pattern as an ensemble of 30 ms spiketrains (0 or 1 spike per input channel, i.e. akin to a population of ON/OFF neurons but with the time of an input spike carrying some information due to the possibility of temporal

summation) and an output pattern as an ensemble of 200 ms spiketrains, using R with a τ_w of 20 ms to measure the similarity between spatiotemporal patterns (Yim et al., 2014).

Together, past computational studies suggest that the DG could perform pattern separation through different codes, but our investigation is the first to systematically explore and compare pattern separation levels based on diverse coding strategies. It is also the first focusing on time codes. Thanks to our slice-based pattern separation assay, we could control input patterns while recording the output of the DG, thus allowing us to experimentally test pattern separation in the DG for the first time (Madar et al., 2018; Santoro, 2013). We considered activity patterns (for both input and output) to be two-second long spiketrains, and used multiple definitions of spiketrain similarity at timescales going from submillisecond to second resolution. We first measured spikecount correlations with R and NDP, two common metrics with different sets of assumptions on the neural code (e.g. NDP doesn't consider common periods of silence as correlated; see **Supplements**), showing that the DG performs decorrelation and orthogonalization of its outputs at subsecond timescales at the level of single GCs (**Figure 3A-B**). Because this phenomenon is stronger at millisecond timescales, and that R and NDP are mostly sensitive to binwise synchrony, we measured spiketrain similarity with SPIKE, assuming a synchrony code purely based on spike times instead of spike counts (Kreuz et al., 2013). This confirmed that GC outputs are separated through "desynchronization" of their spike times from sweep to sweep (**Figure 3D**). Moreover, we designed a new simple similarity metric SF (which complements NDP in the description of the similarity between two spikecount vectors), as well as two complementary measures of spiketrain "burstiness" (compactness and occupancy). These revealed that, in addition to desynchronization strategies, GCs can exhibit pattern separation through firing rate or burstiness codes, and that depending on the timescale, the neural code

considered and the input statistical structure, different levels of pattern separation or convergence are performed (**Figure 6**).

In conclusion, our work demonstrates that single neuron pattern separation can be achieved in isolated hippocampal tissue through multiplexed coding, which is a way of simultaneously representing several features of a stimulus or, in our case, simultaneously performing different computations, through different temporal scales and spiketrain features (Mease et al., 2017; Panzeri et al., 2010; Ratté et al., 2013). Our work illustrates the importance of considering multiple neural codes when studying neuronal computations for three reasons: 1) The fact that conceptually different metrics lead to converging results bolsters our conclusion that temporal pattern separation occurs within the DG and CA3 at the level of single neurons; 2) a single neuron can exhibit either pattern convergence or separation depending on the coding scheme; 3) a given neural code can be more relevant for pattern separation/convergence in certain celltypes than others.

In the future, experiments correlating mnemonic discrimination and generalization with the levels of pattern separation or convergence through various potential codes will help pinpoint which computations are actually used to support episodic memory.

Network mechanisms supporting hippocampal computations

Our work, in showing that spiking was difficult to elicit in GCs and that their responses were sparser than their inputs (**Figure 5**) is in line with past research (Dieni et al., 2016; Mongiat et al., 2009). It also resonates with the long-standing idea that the DG acts as the gate of the hippocampus, filtering out incoming cortical activity before it reaches CA3 to prevent overexcitation (Dengler & Coulter, 2016). Figuring out the computations of the DG is equivalent

to reverse-engineering the transfer function defining the DG filter. Some have suggested that the DG is a low-pass (Pardi et al., 2015; Scullin & Partridge, 2012) or a ~10 Hz band-pass filter (Ewell & Jones, 2010). Our results confirm that the output frequency of GCs is constrained in a narrow band (**Figure 5B**) and go one step further by providing the first demonstration that the filtering properties of the DG allow it to perform different computations including pattern separation in response to complex naturalistic inputs (**Figure 6**).

The question is then: how are these filtering properties implemented? The physiological mechanisms underlying DG computations in general are understudied and remain a mystery. In Madar et al. (2018), we provided a proof-of-principle that the short-term dynamics of synaptic transmission at the perforant path-GC synapses could explain the levels of temporal pattern decorrelation in the DG. But GCs also receive feedforward and feedback inhibition and excitation from multiple interneurons that also interact between each other (Amaral et al., 2007; Ramaswamy, 2015; Scharfman, 2016). Indeed, our finding that partial block of $GABA_A$-mediated neurotransmission impairs temporal pattern separation in the DG (**Figure 7**) strongly suggests that the computations we investigated are network phenomena. Interactions between multiple celltypes are likely involved, and it is thus critical to characterize the suprathreshold input-output transformation of each celltype to parse out their computational role. In the present work, we shed light on the computations of dentate FSs (also known as basket cells providing fast feedforward and feedback perisomatic inhibition to GCs (Hu et al., 2014)), HMCs (glutamatergic interneurons providing feedback monosynaptic excitation and disynaptic inhibition to GCs mostly outside of the lamellar plane (Scharfman, 2016)), and CA3 PCs, the output neurons of the hippocampal subnetwork directly downstream of the DG in the trisynaptic circuit, but which can also provide indirect feedback to the DG via collaterals targeting hilar

neurons (Scharfman, 2016). We discovered that, in contrast to GCs (**Figure 8-9**, and see (Madar et al., 2018)): 1) FSs generally exhibit low levels of pattern separation through binwise desynchronization (R, NDP) or scaling (SF, likely due to high firing rates), but high levels of separation through simple variation of local firing rates from sweep to sweep, especially at the 100 ms timescale and higher; 2) HMCs exhibit intermediate to low levels of orthogonalization up to the 500 ms timescale. However, contrarily to GCs and FSs, they are able to achieve high levels of pattern separation through scaling, thanks to a variable bursting response and low overall firing rates; 3) CA3 PCs exhibit high levels of pattern separation through all tested neural codes, but significantly more than their GC controls through orthogonalization only, especially at long timescales, suggesting that CA3 might complement and amplify the separation inherited from the DG, possibly to make pattern completion more efficient (Madar et al., 2018). In the future, computational modelling combining those results with knowledge of the synaptic dynamics between these populations of neurons will help dissect the role played by each in hippocampal computations.

Our study especially calls for more work on the computational role of inhibitory synaptic dynamics as it reveals the first experimental evidence that fast GABAergic transmission favors pattern separation through multiple neural codes (binwise desynchronization and scaling) and impairs it through another code (occupancy variations at short timescales) (**Figure 7**). Past research has long suspected the importance of inhibition to hippocampal computations. Computational models of the DG implementing perisomatic feedforward inhibition (provided by FSs) in the form of a "k-winners take all" rule controlling the number of GCs activated by a given input pattern have stressed the importance of such inhibition on pattern separation through a population code (Myers & Scharfman, 2009; O'Reilly & McClelland, 1994; Temprana et al.,

2015). The seminal model of Myers and Scharfman (2009) also suggested that certain hilar interneurons, providing feedforward and feedback inhibition on the distal dendrites of GCs, could impair population pattern separation through their influence on other GABAergic interneurons (see also Danielson et al. 2017). Experimentally, a recent behavioral study on mice showed that normal levels of tonic inhibition in GCs are critical for mnemonic discrimination (Engin et al., 2015). Our results now demonstrate that inhibition is also critical for computations that could support this episodic memory function. Future experiments will need to clarify the exact role of different interneuron populations as well as different types of inhibition (e.g. feedforward vs feedback or somatic vs dendritic).

Figures

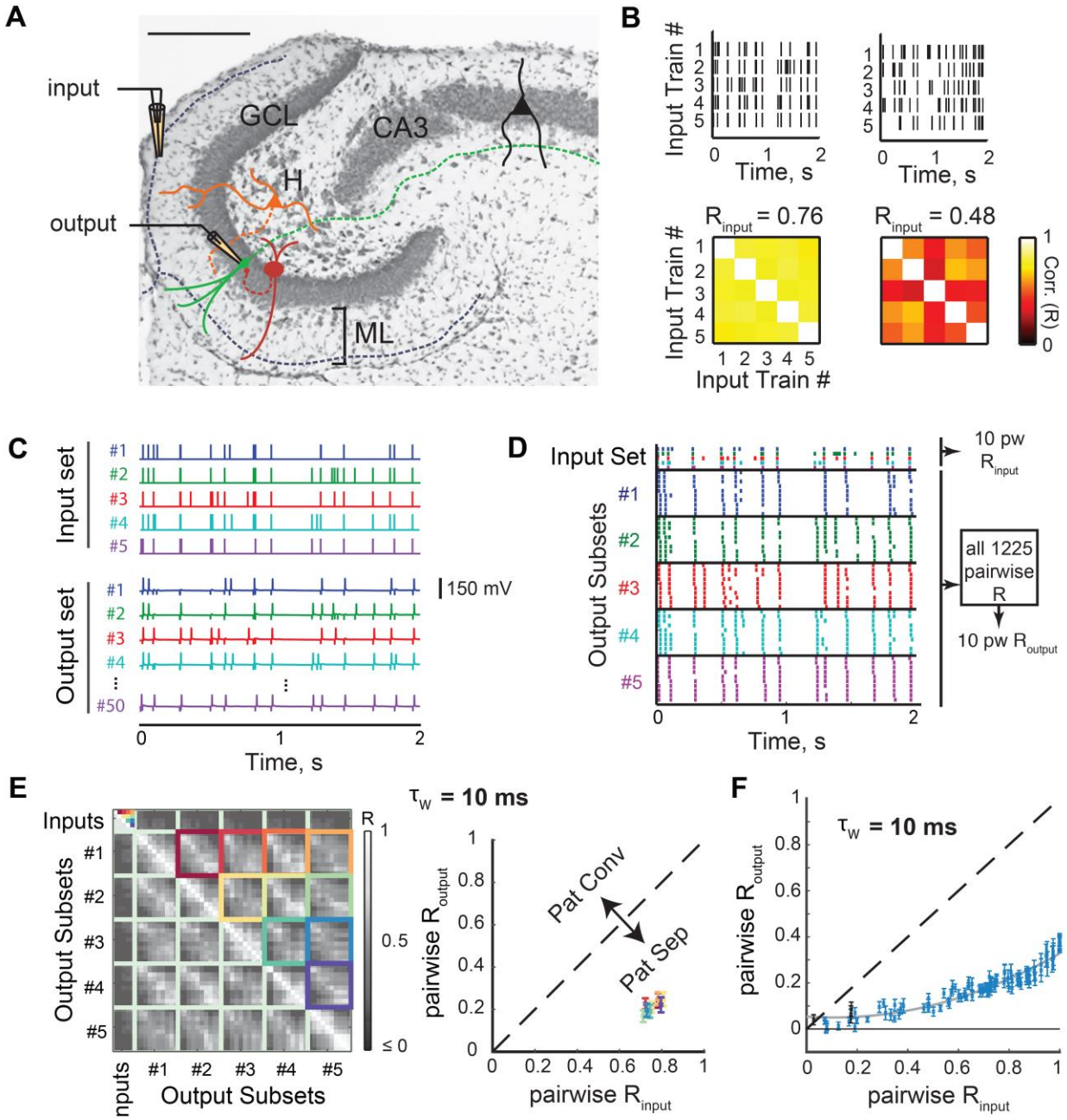

Figure 1. Temporal pattern decorrelation at the level of single dentate granule cells.
(A) Histology of the DG in a horizontal slice (Cresyl violet/Nissl staining; scale bar: 250 µm), overlaid with a schematic of the experimental setup: a theta pipette in the ML is used to focally stimulate the perforant path (input) while a responding GC is recorded via whole-cell patch-clamp (output). GCL: granule cell layer, H: hilus, ML: molecular layer. Celltype color code: green for granule cell (GC); red for fast spiking interneuron (FS); orange for hilar mossy cell (HMC); black for CA3 pyramidal cell. Solid lines represent dendrites and dashed lines axons

(B) Examples of input sets. *Top*: each input set is constituted of five different trains of electrical pulses following a Poisson distribution and an average rate of 10 Hz. *Bottom*: correlation coefficient matrix for each input set, each square is the Pearson's correlation coefficient (R) between two input trains considered as vectors of spike counts with a binning window (τ_w) of 10 ms. R_{input} is the average of coefficients, diagonal excluded. We used 11 such input sets (R_{input} = 0.11 to 1).

(C) Current-clamp recordings of the membrane potential of a single GC in response to a single input set (average R_{input} = 0.76). Each input set (five input trains) is repeated ten times, yielding a recording set of fifty output voltage traces.

(D) Sorted input and output rasters from the recording set in C (each parent input train has ten children output trains forming an output subset, with matching colors). PW means pairwise.

(E) *Left*: Corresponding 55x55 correlation coefficients matrix using a τ_w of 10 ms. Each small grey square represents the correlation coefficient between two spiketrains. The average of coefficients from children output trains corresponding to one of the ten pairs of input trains (identified by color-coded squares), was computed to yield ten pairwise R_{output} coefficients. This excludes comparisons between outputs generated from the same parent input. *Right*: mean across multiple cells, following the same color-code as displayed in the matrix on the left.

(F) Pattern separation graph showing the mean ± SEM pairwise R_{output} across 102 recordings (from 28 GCs), for 11 different input sets (i.e. 110 pairwise R_{input}). Values under the identity line (dashed) demonstrate that output spiketrains were less similar to each other than inputs, and thus that pattern separation was performed. Blue indicates significant difference from the identity line (one-sample t-test on the difference pairwise R_{input} - pairwise R_{output}, $p < 0.05$). The solid grey line is a parabolic fit to the 102 recording sets.

[Figure adapted from Madar et al. (2018) (fig. 1, 2, 5)]

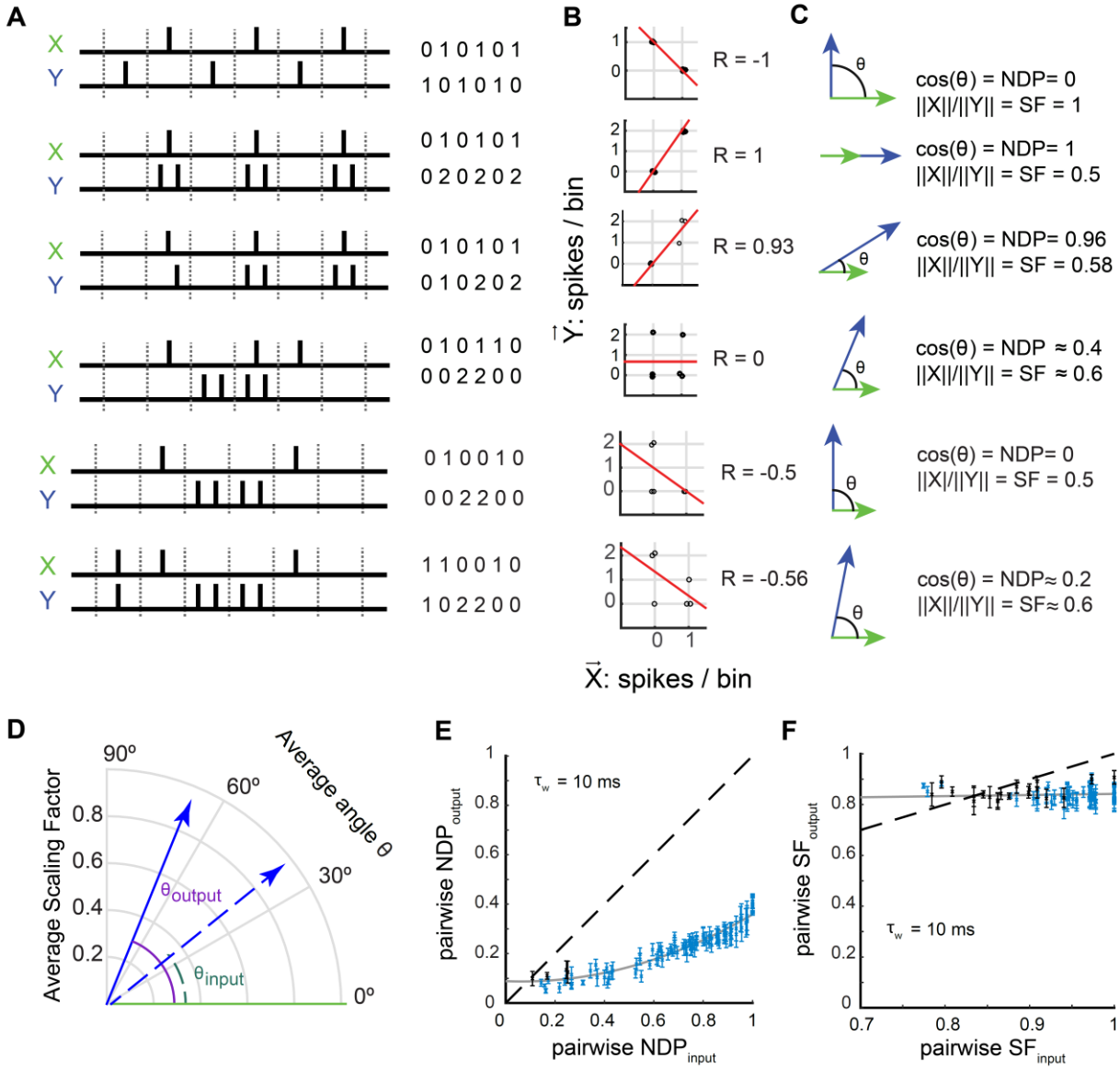

Figure 2. Orthogonalization of input spiketrains is a strong component of temporal pattern separation by single granule cells.

(A-C) Six hypothetical cases of pairs of spiketrains and their associated Pearson's correlation coefficients (R), normalized dot products (NDP, cosine of the angle between two vectors) and scaling factors (SF, ratio of the norms), showing that the three metrics assume different neural codes and are not equivalent. **(A)** Synthetic spiketrains (X and Y pairs) divided into six bins, with the corresponding number of spikes per bin. **(B)** R between each pair of X and Y describes the linear regression between the number of spikes in the bins of X versus the corresponding bins in Y (jitter was added to make all points visible). **(C)** Geometric view of vectors X and Y, where each bin is a dimension of a 6-dimensional space, and the number of spikes in a bin is the coordinate along this dimension. NDP measures how far from orthogonal two spiketrains are and SF measures how different their binwise firing rates are. (**A-C)** NDP and R are sensitive to whether spiketrains have spikes in the same bins or not (row 1), whereas SF is sensitive to differences in spikecounts per bin (row 2), although neither NDP nor R is purely about "bin synchrony" (row 3). Note that these examples provide the intuition that orthogonal vectors (NDP = 0) necessarily correspond to a negative correlation between the spiketrains (row 1 and 5) but that anticorrelated

spiketrains ($R < 0$) are not necessarily orthogonal (row 6), and that orthogonal spiketrains are not necessarily perfectly anticorrelated as in row 1 because R, unlike NDP, considers common silent bins as correlated (row 5). See also **Figure S1.**

(D) Vector representation of experimental data from one recording set, showing the average similarity between a set of input spiketrains (dashed line and green angle, $R_{input} = 0.76$) and the average similarity between the fifty corresponding output spiketrains excluding comparisons between outputs from same parent input (solid line, purple angle). The angles are derived from the NDP whereas the lengths of each vector express differences in binwise firing rates (SF). Here, outputs are more orthogonal (closer to 90˚) than their inputs with little difference in scaling.

(E-F) Pattern separation graphs showing the pairwise output similarity as a function of the pairwise input similarity, as measured by the NDP or SF (mean+/-SEM) across 102 recording sets (28 GCs) for 11 different input sets. As in Figure 1F, blue indicates a significant difference from the identity line (one-sample t-test, $p < 0.05$). The solid grey line is a parabolic (E) or linear (F) fit to the 102 recording sets. **(E)** Outputs are closer to orthogonality (NDP = 0) than their respective inputs, demonstrating strong levels of pattern separation through orthogonalization at the 10 ms timescale. **(F)** At the 10 ms timescale, pattern separation by scaling is present for inputs very similar in terms of SF (SF_{input} close to 1), but weak, at least over the span of tested SF_{input} values.

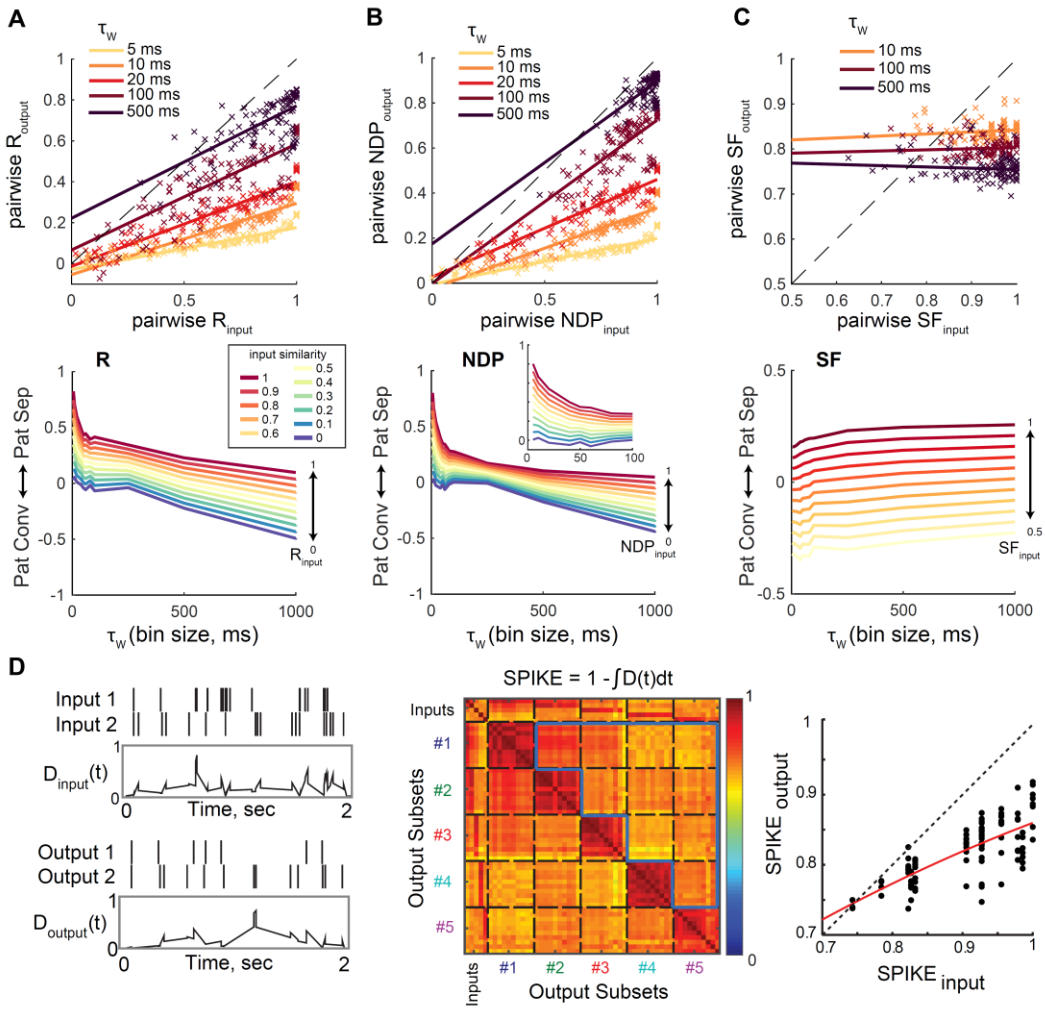

Figure 3. Single granule cells exhibit pattern separation on millisecond to second timescales using different codes.

(A-C) Pattern separation/convergence assessed at different timescales and using different measures of similarity (S). *Top*: pairwise S_{output} (average across recording sets) as a function of pairwise S_{input}, measured with different binning windows τ_w. Solid curves are linear fits. Each color corresponds to a different τ_w ranging from 10 ms to 500 ms. *Bottom*: Effect of τ_w on the effective decorrelation ($S_{input} - S_{output}$), interpolated from the linear regressions. Note that as τ_w increases, pattern separation through decorrelation (R) or orthogonalization (NDP) becomes weaker while it becomes stronger through scaling (SF). **(D)** Similarity between spiketrains is here assessed with the binless SPIKE metric, directly using spike times. *Left*: example of two input spiketrains associated with two output spiketrains from a GC recording set, and the corresponding distances D(t) between spiketrains. D(t) can then be integrated over time to give a single value D. *Middle:* example of 55x55 matrix of SPIKE similarity (1-D) between all spiketrains of an example recording set. 0 means that spikes of two trains never happened close in time, and 1 that they were perfectly synchronous. The output SPIKE similarity ($SPIKE_{output}$) is defined as the average similarity excluding comparisons between spiketrain from the same parent input train (i.e. average of the 10 pairwise $SPIKE_{output}$). *Right*: $SPIKE_{output}$ of the same 102 GC recordings as in Figure 1-3, as a function of $SPIKE_{input}$, fitted with a parabola (red line). Most data points are below the dashed identity line indicating that output spiketrains are less similar than inputs. The average $SPIKE_{input}$-$SPIKE_{output}$ is significantly above 0 for all input sets except the two most dissimilar ($SPIKE_{input}$ = 0.74, 0.78) (one-sample T-tests, $p < 0.05$).

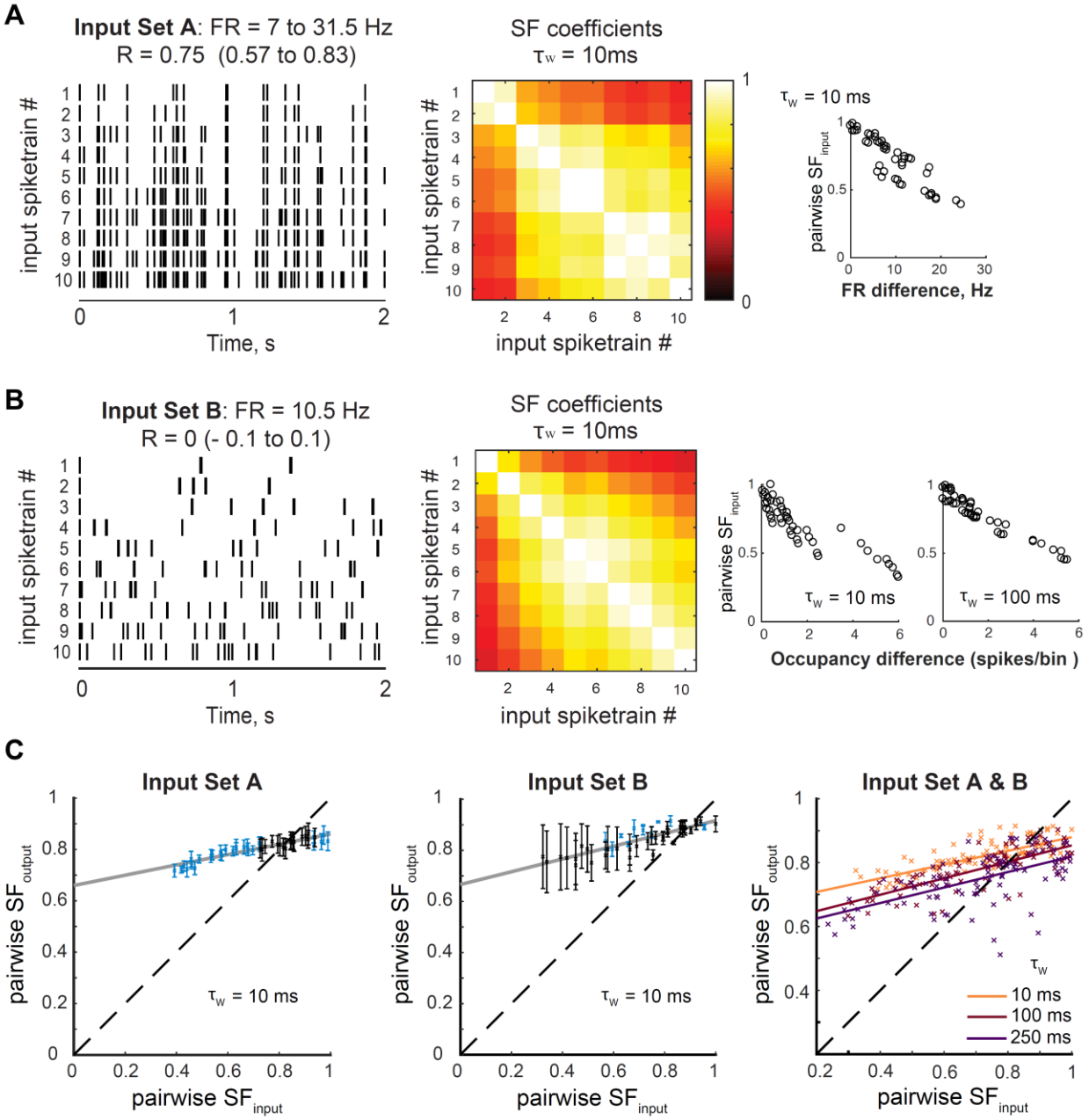

Figure 4. Pattern convergence via scaling in single granule cells.
(A-B) Two new input sets were designed to explore single GCs computations on inputs with a wide range of pairwise similarity as measured by SF. Both input sets have ten input trains of 2 s, and were repeated five times during the whole-cell patch-clamp recording of a single GC, yielding 50 output spiketrains.
(A) *Left*: Input set A was constituted of spiketrains following a Poisson distribution, each with a different firing rate (FR), increased from 7 to 31.5 Hz, but with an average R_{input} constrained around 0.75 (τ_w = 10 ms). The ten input trains were thus well correlated but varied in their firing rate. *Middle*: matrix of SF coefficients for each pair of trains in input set A, showing a wide range of values unlike the 11 input sets with 10 Hz trains used in previous experiments. *Right*: SF values are indeed sensitive and anti-correlated to differences in overall firing rate between two spiketrains (data points correspond to pairs of trains).
(B) Because SF is dependent on how differently clustered spikes are in two different trains, SF can vary even when the overall firing rate is the same. *Left*: Input set B was constituted of spiketrains with 21 spikes (FR = 10.5 Hz) that were clustered in more or less bins, leading to trains with varying burstiness

and thus a wide range of SF values (*Middle*). R was not constrained but ended up close to 0 for all pairs. *Right*: SF values are indeed sensitive and anticorrelated to differences in occupancy (average number of spikes per occupied bins), a direct measure of burstiness when FR is constant across trains (data points correspond to pairs of trains).

(C) Pattern separation graphs showing the pairwise output similarity as a function of the pairwise input similarity, as measured by SF, across 5 GCs responses to input set A and 3 GCs responses to input set B (Both input sets tested GC responses over 45 pairwise R_{input}). *Left and Middle*: Mean+/-SEM. Blue indicates a significant difference from the identity line (one-sample t-test, $p < 0.05$). The solid grey line is a linear fit to the 5x45 (*Left*) or 3x45 (*Middle*) data points. Both experiments confirm that, at the 10 ms timescale, GCs exhibit pattern separation through scaling for highly similar input trains (SF close to 1) as in Figure 2F, but show that GCs can exhibit pattern convergence for more dissimilar inputs (SF < 0.7). *Right*: Mean across GC recordings for both experiments combined, measured at different timescales. It confirms that SF_{output} decreases when using larger binning windows, leading to more pattern separation for high input similarity and lower pattern convergence for lower input similarities.

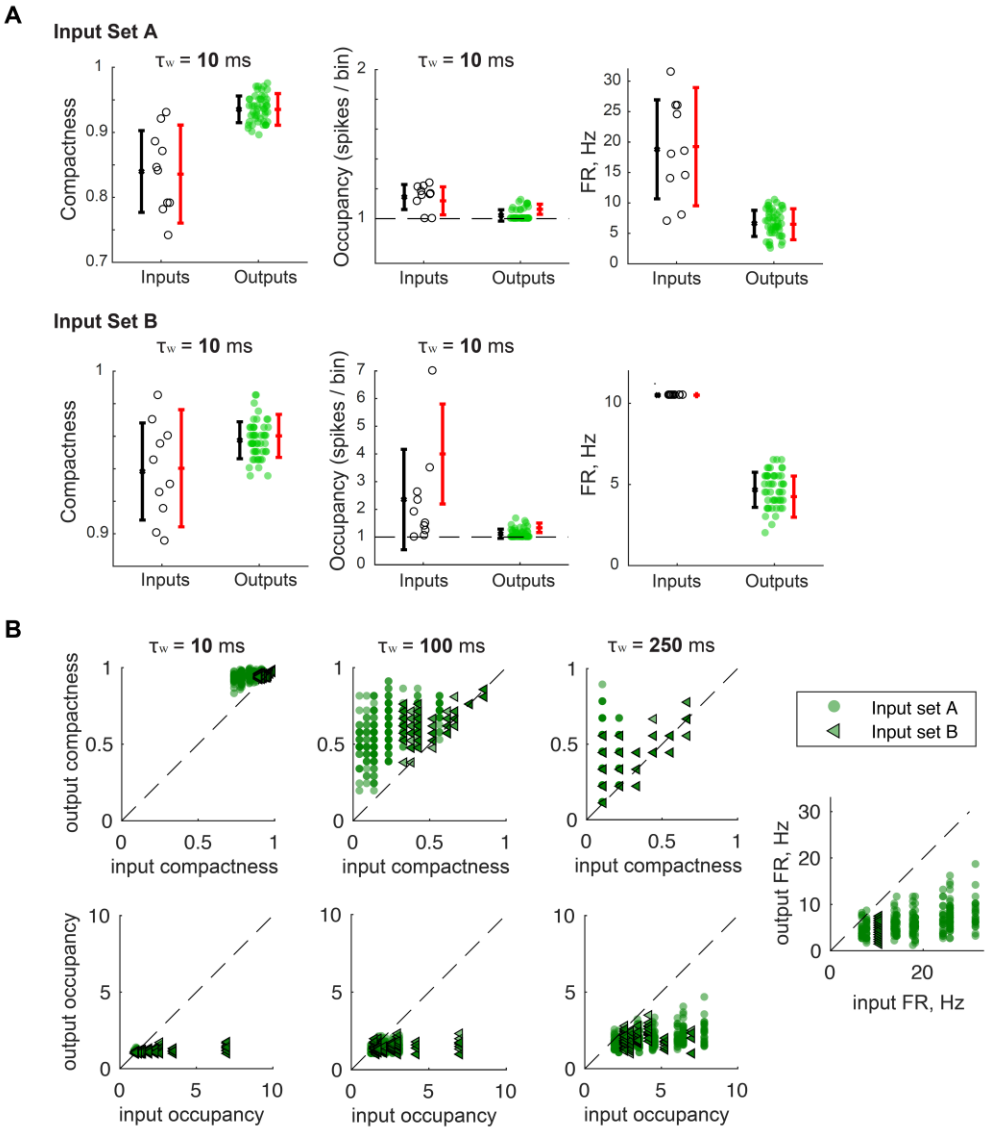

Figure 5. Granule cells input-output transformations in terms of firing rate and burstiness. **(A)** Graphs shown correspond to the same GC in response to either input set A or B. Data points correspond to individual spiketrains, (black empty circles for inputs: 10 trains per set; green filled circles for GC outputs: 50 trains per set). For each spiketrain, we measured its overall FR, binwise compactness and binwise occupancy, all spiketrain features providing information on sparseness and burstiness (see **Methods**). Error bars correspond to two different measures of dispersion. Black: mean +/- SD; red: min-max center of gravity ± the mean absolute difference (self-comparisons and comparisons between output trains with the same parent input train were excluded). Comparing mean values of a given spiketrain feature between inputs and outputs shows the direction of the transformation from inputs to outputs. Comparing the dispersion between inputs and outputs shows whether pattern separation (larger output dispersion) or convergence (smaller output dispersion) was achieved through a neural code focused on the measured spiketrain feature.

(B) For each output spiketrain, the output spiketrain measures of compactness, occupancy or overall FR is plotted against the measure of its parent input train (input set A or B). For all timescales, GCs have generally higher compactness than their inputs, but maintain a low and narrow range of occupancy regardless of their input statistics, showing that GCs are sparser (see **Table S2**). Consistently, GCs maintain a lower FR than their inputs.

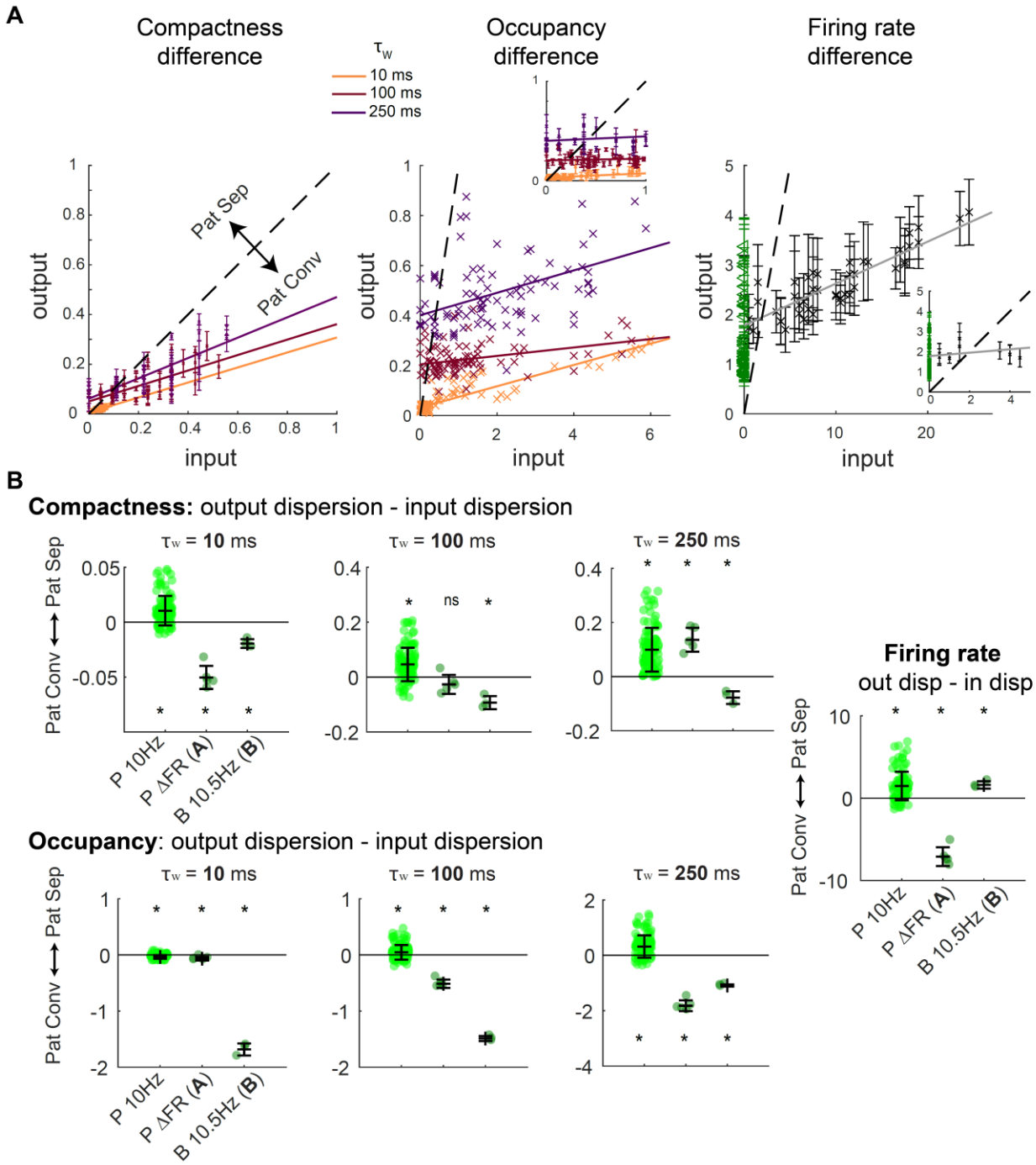

Figure 6. Depending on inputs statistical structure, granule cells exhibit pattern separation or convergence via burstiness and firing rate codes.

(A) Pattern separation graphs showing the average pairwise output absolute difference across GC recordings as a function of the pairwise input absolute difference, for the binwise compactness (*Left*), binwise occupancy (*Middle*) and overall FR (*Right*). Insets zoom in on the smallest values of the input-axis. Experiments using input set A and B were combined. Note that because we plot the absolute difference between two spiketrains (i.e. the distance between two data points in Figure 5A) and not a measure of similarity, pattern separation corresponds to points above the identity line (dashed) and pattern

convergence to points below. Error bars are SEM (not displayed in middle graph for readability). *Right*: input set A recordings (P ΔFR) in black, input set B (B 10.5 Hz) in green.

(B) The difference in dispersion ($\text{Dispersion}_{\text{output}} - \text{Dispersion}_{\text{input}}$; dispersion is the mean absolute difference, i.e. red bars in Figure 5A) of binwise compactness, binwise occupancy or overall FR for each GC recording set from three experiments using different types of input sets: Poisson trains with 10 Hz FR and varying R (P 10Hz: 102 recordings, 28 GCs), Poisson trains with $R \approx 0.75$ and varying FR (P ΔFR, i.e. input set A: 5 GCs), trains with 10 Hz FR and varying burstiness (B 10.5 Hz, i.e. input set B: 3 GCs). Positive values correspond to pattern separation through variations of the given spiketrain property (compactness, occupancy or FR) and negative values to pattern convergence. Asterisks denote significant difference from 0, i.e. either pattern separation or convergence (one-sample t-test, $p < 0.05$. See **Table 1**).

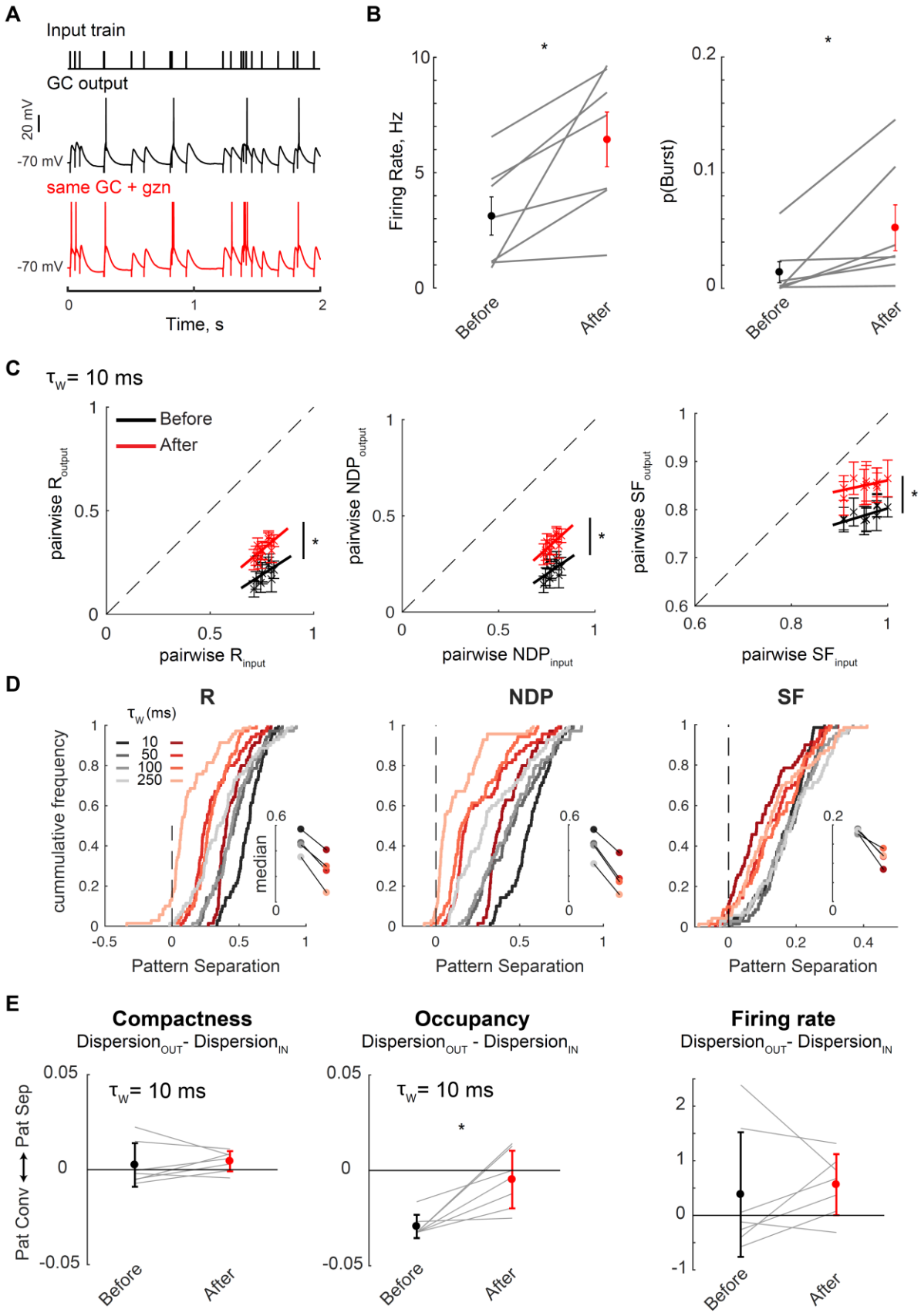
A
Input train
GC output
20 mV
-70 mV
same GC + gzn
-70 mV
0
1
2
Time, s
B
Firing Rate, Hz
10
5
0
*
Before
After
p(Burst)
0.2
0.1
0
*
Before
After
C
τW= 10 ms
Before
After
pairwise Routput
pairwise Rinput
pairwise NDPoutput
pairwise NDPinput
pairwise SFoutput
pairwise SFinput
*
D
R
NDP
SF
τW (ms)
10
50
100
250
cummulative frequency
median
Pattern Separation
E
Compactness
Dispersion_OUT - Dispersion_IN
Occupancy
Dispersion_OUT - Dispersion_IN
Firing rate
Dispersion_OUT - Dispersion_IN
τW= 10 ms
Pat Conv ⟷ Pat Sep
Before
After

926

Figure 7. Inhibition controls levels of pattern separation in granule cells through different neural codes

(A) Single GCs were recorded twice in response to the same input set (P 10 Hz, R = 0.76 at τ_w = 10 ms, shown in Figure 1B): First in normal aCSF, then under conditions of partial inhibitory block (aCSF + 100 nM gabazine, gzn), without changing any other parameter (i.e. same stimulation location and intensity).

(B) Partial disinhibition of GCs led to higher FR and a higher propensity to fire small bursts of spikes riding on the same EPSP, as illustrated in A and evidenced by an increased p(Burst) (probability of firing more than one spike between two input pulses). FR and p(Burst) were computed for each recording set (n = 7 GCs). Paired t-test (FR and p(Burst) respectively): p = 0.02, p = 0.04.

(C) Pattern separation graphs showing the pairwise output similarity as a function of the pairwise input similarity, as measured by R, NDP or SF at the 10 ms timescale (mean+/-SEM) across recordings in 7 GCs. Data points below the identity line (dashed) correspond to pattern separation. Partial block of inhibition in GCs led to a significant decrease in pattern separation through all similarity metrics (ANCOVA with separate-lines model fitting 70 data points per treatment group: $p < 0.0001$). Solid lines are the linear fits used for the ANCOVA.

(D) Cumulative frequency distributions of the distance of (pairwise S_{input}, pairwise S_{output}) data points to the identity line in pattern separation graphs as in C (insets show medians). Positive values of the x-axis correspond to pattern separation, and negative values to pattern convergence. Red curves (after gzn) are all shifted to the left of their black counterparts (before gzn), showing a decrease in pattern separation at all timescales. The shift is more pronounced at larger timescales for R and NDP, at smaller timescales for SF. ANCOVA on (pw S_{input}, pw S_{output}) data points with separate-lines model: $p < 0.0001$ for τ_w up to 1000 ms for R and NDP, $p < 0.02$ for SF.

(E) Average levels of pattern separation via compactness, occupancy or FR codes were measured for each recording set (as in Figure 6B). Surprisingly, partial block of inhibition did not significantly change the variations in FR or binwise compactness of output spiketrains, but it led to less pattern convergence or even pattern separation through variations of occupancy (paired t-test: p = 0.008, 0.024, 0.031 for τ_w = 10, 20 and 50 ms respectively. No significant difference between treatments for larger τ_w or other spiketrain features at any τ_w.

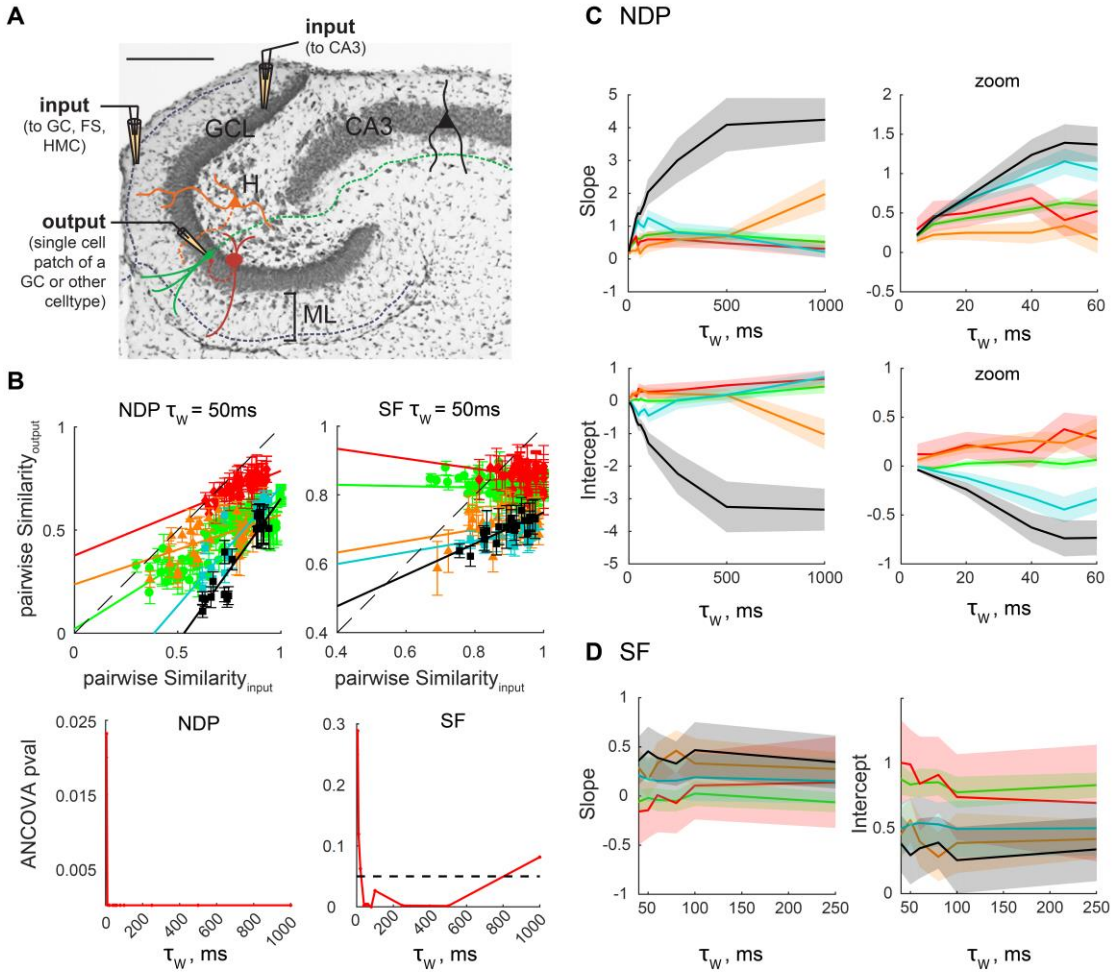

Figure 8. Levels of pattern separation through orthogonalization and scaling differ between hippocampal celltypes.

(A) Temporal pattern separation assays were performed by single whole-cell current-clamp recordings from GCs (green, same experiments as Figure 1-3), FSs (red), HMCs (orange) and CA3 PCs (black). For GCs, FSs and HMCs, input sets with Poisson trains of 10 Hz FR (e.g. Figure 1B) were delivered by stimulating in the outer molecular layer (OML)**.** For CA3 PCs those stimulus parameters rarely if ever elicited spiking, therefore input sets were constituted of Poisson trains with a 30 Hz FR delivered in the GCL, and recordings were performed under partial block of inhibition (100 nM Gabazine). Control experiments (teal) were performed in GCs under the same pharmacological conditions and 30 Hz input sets, but the stimulations were delivered in the OML. The membrane potential was maintained around -70 mV (between -70 and -60 mV for CA3 PCs).

(B) Pattern separation graphs showing the pairwise output similarity as a function of the pairwise input similarity, as measured by NDP or SF at the 50 ms timescale (mean+/-SEM: 28 GCs, 3-13 recordings per input set; 4 FSs, 4 recordings per input set; 11 HMCs, 5-7 recordings per input set; 14 CA3 PC + gzn, 6-9 recordings per input set; 13 control GCs + gzn, with 11 recordings per input set). Same color code as in A. Data points below the identity line (dashed) correspond to pattern separation. All celltypes performed pattern separation through both orthogonalization and scaling but with different levels (ANCOVA with separate-lines model: p-values for different timescales plotted in the *bottom* graphs. Dashed horizontal line is significance level at 0.05). Solid lines are the linear fits used for the ANCOVA.

(C-D) Slope and intercept of the linear models used to fit (S_{input}, S_{output}) data points for a given celltype and timescale. The shaded patches correspond to the 95% confidence interval of the parameter estimate

from the ANCOVA regression. This analysis details how pattern separation functions differ between celltypes.

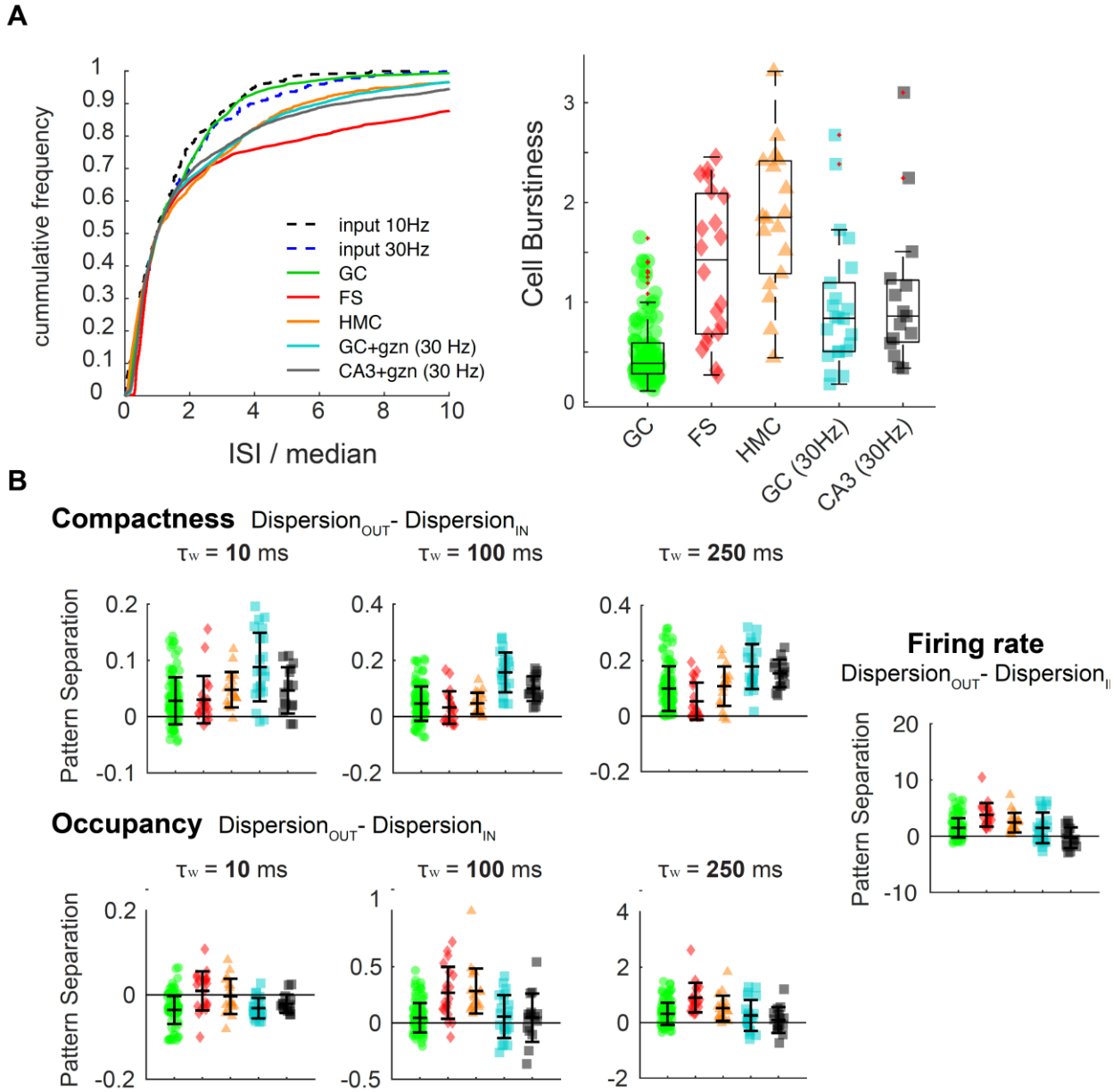

Figure 9. Levels of pattern separation and convergence through burstiness and firing rate codes differ between hippocampal celltypes.

(A) Assessment of burstiness in different celltypes (binless analysis).

Left: Cumulative frequency distributions of interspike intervals (ISI) observed in the output spiketrains of different hippocampal celltypes and their associated input trains. ISI of all recordings of a given celltype or input set type were pooled. The ISIs were normalized to their median for a given celltype or input type, such that their cumulative distribution would cross at frequency = 0.5, and that all exponential distributions (characteristic of a Poisson process, as both type of input sets are) would be super-imposed or very close to each other. Thus, GC are visually close to an exponential distribution, suggesting their output is not bursty. Distributions falling away from their exponential input distribution suggest that spikes are organized in a non-Poisson manner, suggestive of a bursty behavior. In this sense, HMCs, CA3 PCs and their GC controls seem to exhibit a similar bursty behavior, and FSs an even more bursty one.

Right: Quantification of the burstiness of each recording set (102 for GCs, 20 for FSs, 18 for HMCs, 15 for CA3 PCs+gzn and 22 for GCs+gzn). Burstiness was assessed as the Kullback-Leibler divergence from P to M, with M the frequency distribution of normalized ISI in an output set (50 output trains), and P the frequency distribution of normalized ISI in the associated input set type (either Poisson 10Hz or Poisson 30 Hz input sets were combined, as in A). The higher the divergence, the burstier a cell is. This analysis confirms that GCs outputs are close to a Poisson process, and that all other celltypes and conditions are significantly burstier (Kruskal-Wallis one-way ANOVA: $p < 0.0001$; post-hoc t-tests with Tukey-Kramer correction $p < 0.01$ for all GC (10Hz) to other celltypes comparisons. CA3 PCs and GC controls (30Hz) are not significantly different ($p = 0.99$) nor FSs and HMCs ($p = 0.64$)). Box plots: central mark and edges are the median, the 25th and the 75th percentiles, respectively. Whiskers are most extreme data points not considered outliers (red +).

(B) Average levels of pattern separation via binwise compactness, binwise occupancy or FR codes were measured for each recording set of every celltype, as in Figure 6B (negative values indicate pattern convergence). Levels were different between celltypes (Kruskal-Wallis one-way ANOVA: $p < 0.0001$; post-hoc t-tests with Tukey-Kramer correction for multiple comparisons in **Table 2**). This analysis shows that FSs and HMCs achieve more pattern separation through variations of occupancy and FR, whereas CA3 PCs (30Hz) and GC controls (30 Hz) achieve more pattern separation through variations of compactness.

Table 1 related to Figure 6B

One sample t-test (difference from 0)
p value < 0.05 in red.

	τ_w = 10 ms	τ_w = 100 ms	τ_w = 250 ms	
Input set		**Compactness**		
P 10 Hz	< 0.0001	< 0.0001	< 0.0001	
P ΔFR	0.0004	0.1576	0.0023	
B 10.5 Hz	0.0135	0.0213	0.0298	
		Occupancy		**Firing rate**
P 10 Hz	< 0.0001	0.0004	< 0.0001	< 0.0001
P ΔFR	0.0095	< 0.0001	< 0.0001	0.00016
B 10.5 Hz	0.0014	0.0003	0.00048	0.0244

Table 2 related to Figure 9B

Posthoc Tukey-Kramer test on means after Kruskal-Wallis one-way ANOVA (p value < 0.05 in red).

Compared Celltypes		τ_w = 10 ms	τ_w = 100 ms	τ_w = 250 ms	
			Compactness		
GC	FS	1	0.8171	0.1582	
GC	HMC	0.1498	0.9995	0.9421	
GC	GC+gzn	0.0001	< 0.0001	0.0005	
GC	CA3+gzn	0.4537	0.0075	0.0275	
FS	HMC	0.3524	0.8609	0.1452	
FS	GC+gzn	0.0049	< 0.0001	< 0.0001	
FS	CA3+gzn	0.6357	0.0046	0.0006	
HMC	GC+gzn	0.5703	0.0004	0.1205	
HMC	CA3+gzn	0.9967	0.0952	0.393	
GC+gzn	CA3+gzn	0.3859	0.6809	0.9938	
			Occupancy		**Firing rate**
GC	FS	0.0001	0.0001	< 0.0001	< 0.0001
GC	HMC	0.0108	< 0.0001	0.4431	0.23
GC	GC+gzn	1	0.9936	0.9254	0.9997
GC	CA3+gzn	0.3589	0.9997	0.394	0.0478
FS	HMC	0.9074	0.962	0.1825	0.3698
FS	GC+gzn	0.0039	0.0164	0.0002	0.0016
FS	CA3+gzn	0.3906	0.027	< 0.0001	< 0.0001
HMC	GC+gzn	0.0827	0.002	0.2858	0.3648
HMC	CA3+gzn	0.8891	0.0042	0.0653	0.0021
GC+gzn	CA3+gzn	0.5975	0.9999	0.9029	0.2075

References

Adrian, E. D. (1928). *The basis of sensation*: Christophers; London, 22 Berners Steeet, W. 1.

Aimone, J. B., Wiles, J., & Gage, F. H. (2009). Computational influence of adult neurogenesis on memory encoding. *Neuron, 61*(2), 187-202. doi: 10.1016/j.neuron.2008.11.026

Amaral, D. G., Scharfman, H. E., & Lavenex, P. (2007). The dentate gyrus: fundamental neuroanatomical organization (dentate gyrus for dummies). *163*, 3-790. doi: 10.1016/s0079-6123(07)63001-5

Berger, T. W., Eriksson, J. L., Ciarolla, D. A., & Sclabassi, R. J. (1988a). Nonlinear systems analysis of the hippocampal perforant path-dentate projection. II. Effects of random impulse train stimulation. *J Neurophysiol, 60*(3), 1076-1094.

Berger, T. W., Eriksson, J. L., Ciarolla, D. A., & Sclabassi, R. J. (1988b). Nonlinear systems analysis of the hippocampal perforant path-dentate projection. III. Comparison of random train and paired impulse stimulation. *J Neurophysiol, 60*(3), 1095-1109. doi: 10.1152/jn.1988.60.3.1095

Berron, D., Schutze, H., Maass, A., Cardenas-Blanco, A., Kuijf, H. J., Kumaran, D., & Duzel, E. (2016). Strong Evidence for Pattern Separation in Human Dentate Gyrus. *J Neurosci, 36*(29), 7569-7579. doi: 10.1523/jneurosci.0518-16.2016

Bliss, T. V., & Lomo, T. (1973). Long-lasting potentiation of synaptic transmission in the dentate area of the anaesthetized rabbit following stimulation of the perforant path. *J Physiol, 232*(2), 331-356.

Chacron, M. J., Longtin, A., & Maler, L. (2001). Negative interspike interval correlations increase the neuronal capacity for encoding time-dependent stimuli. *J Neurosci, 21*(14), 5328-5343.

Chavlis, S., Petrantonakis, P. C., & Poirazi, P. (2017). Dendrites of dentate gyrus granule cells contribute to pattern separation by controlling sparsity. *Hippocampus*.

Chavlis, S., & Poirazi, P. (2017). Pattern separation in the hippocampus through the eyes of computational modeling. *Synapse*. doi: 10.1002/syn.21972

Colgin, L. L., Moser, E. I., & Moser, M. B. (2008). Understanding memory through hippocampal remapping. *Trends Neurosci, 31*(9), 469-477. doi: 10.1016/j.tins.2008.06.008

Cook, E. P., Guest, J. A., Liang, Y., Masse, N. Y., & Colbert, C. M. (2007). Dendrite-to-soma input/output function of continuous time-varying signals in hippocampal CA1 pyramidal neurons. *J Neurophysiol, 98*(5), 2943-2955. doi: 10.1152/jn.00414.2007

Cotterill, E., Charlesworth, P., Thomas, C. W., Paulsen, O., & Eglen, S. J. (2016). A comparison of computational methods for detecting bursts in neuronal spike trains and their application to human stem cell-derived neuronal networks. *J Neurophysiol, 116*(2), 306-321. doi: 10.1152/jn.00093.2016

Danielson, N. B., Turi, G. F., Ladow, M., Chavlis, S., Petrantonakis, P. C., Poirazi, P., & Losonczy, A. (2017). In Vivo Imaging of Dentate Gyrus Mossy Cells in Behaving Mice. *Neuron, 93*(3), 552-559. e554.

Dengler, C. G., & Coulter, D. A. (2016). Normal and epilepsy-associated pathologic function of the dentate gyrus. *Prog Brain Res, 226*, 155-178. doi: 10.1016/bs.pbr.2016.04.005

Destexhe, A., Rudolph, M., & Pare, D. (2003). The high-conductance state of neocortical neurons in vivo. *Nat Rev Neurosci, 4*(9), 739-751. doi: 10.1038/nrn1198

Dettner, A., Munzberg, S., & Tchumatchenko, T. (2016). Temporal pairwise spike correlations fully capture single-neuron information. *Nat Commun, 7*, 13805. doi: 10.1038/ncomms13805

Dieni, C. V., Panichi, R., Aimone, J. B., Kuo, C. T., Wadiche, J. I., & Overstreet-Wadiche, L. (2016). Low excitatory innervation balances high intrinsic excitability of immature dentate neurons. *Nat Commun, 7*, 11313. doi: 10.1038/ncomms11313

Dobrunz, L. E., & Stevens, C. F. (1999). Response of hippocampal synapses to natural stimulation patterns. *Neuron, 22*(1), 157-166.

Eichenbaum, H. (2017). On the integration of space, time, and memory. *Neuron, 95*(5), 1007-1018.

Elijah, D. H., Samengo, I., & Montemurro, M. A. (2015). Thalamic neuron models encode stimulus information by burst-size modulation. *Front Comput Neurosci, 9*, 113. doi: 10.3389/fncom.2015.00113

Engin, E., Zarnowska, E. D., Benke, D., Tsvetkov, E., Sigal, M., Keist, R., . . . Rudolph, U. (2015). Tonic Inhibitory Control of Dentate Gyrus Granule Cells by alpha5-Containing GABAA Receptors Reduces Memory Interference. *J Neurosci, 35*(40), 13698-13712. doi: 10.1523/jneurosci.1370-15.2015

Ewell, L. A., & Jones, M. V. (2010). Frequency-tuned distribution of inhibition in the dentate gyrus. *J Neurosci, 30*(38), 12597-12607. doi: 10.1523/jneurosci.1854-10.2010

Fellous, J. M., Rudolph, M., Destexhe, A., & Sejnowski, T. J. (2003). Synaptic background noise controls the input/output characteristics of single cells in an in vitro model of in vivo activity. *Neuroscience, 122*(3), 811-829.

Fuhrmann, G., Segev, I., Markram, H., & Tsodyks, M. (2002). Coding of temporal information by activity-dependent synapses. *J Neurophysiol, 87*(1), 140-148.

Gundlfinger, A., Breustedt, J., Sullivan, D., & Schmitz, D. (2010). Natural spike trains trigger short- and long-lasting dynamics at hippocampal mossy fiber synapses in rodents. *PLoS One, 5*(4), e9961. doi: 10.1371/journal.pone.0009961

Gutig, R. (2014). To spike, or when to spike? *Curr Opin Neurobiol, 25*, 134-139. doi: 10.1016/j.conb.2014.01.004

Hainmueller, T., & Bartos, M. (2018). Parallel emergence of stable and dynamic memory engrams in the hippocampus. *Nature*. doi: 10.1038/s41586-018-0191-2

Hayakawa, H., Samura, T., Kamijo, T. C., Sakai, Y., & Aihara, T. (2015). Spatial information enhanced by non-spatial information in hippocampal granule cells. *Cogn Neurodyn, 9*(1), 1-12. doi: 10.1007/s11571-014-9309-x

Hopfield, J. J. (1982). Neural networks and physical systems with emergent collective computational abilities. *Proc Natl Acad Sci U S A, 79*(8), 2554-2558.

Hosp, J. A., Struber, M., Yanagawa, Y., Obata, K., Vida, I., Jonas, P., & Bartos, M. (2014). Morpho-physiological criteria divide dentate gyrus interneurons into classes. *Hippocampus, 24*(2), 189-203. doi: 10.1002/hipo.22214

Hsu, T. T., Lee, C. T., Tai, M. H., & Lien, C. C. (2016). Differential Recruitment of Dentate Gyrus Interneuron Types by Commissural Versus Perforant Pathways. *Cereb Cortex, 26*(6), 2715-2727. doi: 10.1093/cercor/bhv127

Hu, H., Gan, J., & Jonas, P. (2014). Interneurons. Fast-spiking, parvalbumin(+) GABAergic interneurons: from cellular design to microcircuit function. *Science, 345*(6196), 1255263. doi: 10.1126/science.1255263

Hyde, R. A., & Strowbridge, B. W. (2012). Mnemonic representations of transient stimuli and temporal sequences in the rodent hippocampus in vitro. *Nat Neurosci, 15*(10), 1430-1438. doi: 10.1038/nn.3208

Kamijo, T. C., Hayakawa, H., Fukushima, Y., Kubota, Y., Isomura, Y., Tsukada, M., & Aihara, T. (2014). Input integration around the dendritic branches in hippocampal dentate granule cells. *Cogn Neurodyn, 8*(4), 267-276. doi: 10.1007/s11571-014-9280-6

Kepecs, A., & Lisman, J. (2003). Information encoding and computation with spikes and bursts. *Network, 14*(1), 103-118.

Kirwan, C. B., Hartshorn, A., Stark, S. M., Goodrich-Hunsaker, N. J., Hopkins, R. O., & Stark, C. E. (2012). Pattern separation deficits following damage to the hippocampus. *Neuropsychologia, 50*(10), 2408-2414. doi: 10.1016/j.neuropsychologia.2012.06.011

Kreuz, T., Chicharro, D., Houghton, C., Andrzejak, R. G., & Mormann, F. (2013). Monitoring spike train synchrony. *J Neurophysiol, 109*(5), 1457-1472. doi: 10.1152/jn.00873.2012

Krueppel, R., Remy, S., & Beck, H. (2011). Dendritic integration in hippocampal dentate granule cells. *Neuron, 71*(3), 512-528. doi: 10.1016/j.neuron.2011.05.043

Lee, C. T., Kao, M. H., Hou, W. H., Wei, Y. T., Chen, C. L., & Lien, C. C. (2016). Causal Evidence for the Role of Specific GABAergic Interneuron Types in Entorhinal Recruitment of Dentate Granule Cells. *Sci Rep, 6*, 36885. doi: 10.1038/srep36885

Legendy, C. R., & Salcman, M. (1985). Bursts and recurrences of bursts in the spike trains of spontaneously active striate cortex neurons. *J Neurophysiol, 53*(4), 926-939. doi: 10.1152/jn.1985.53.4.926

Leutgeb, J. K., Leutgeb, S., Moser, M. B., & Moser, E. I. (2007). Pattern separation in the dentate gyrus and CA3 of the hippocampus. *Science, 315*(5814), 961-966. doi: 10.1126/science.1135801

Lin, L., Osan, R., Shoham, S., Jin, W., Zuo, W., & Tsien, J. Z. (2005). Identification of network-level coding units for real-time representation of episodic experiences in the hippocampus. *Proc Natl Acad Sci U S A, 102*(17), 6125-6130. doi: 10.1073/pnas.0408233102

Lisman, J., Buzsaki, G., Eichenbaum, H., Nadel, L., Ranganath, C., & Redish, A. D. (2017). Viewpoints: how the hippocampus contributes to memory, navigation and cognition. *Nat Neurosci, 20*(11), 1434-1447. doi: 10.1038/nn.4661

Lisman, J. E., & Jensen, O. (2013). The theta-gamma neural code. *Neuron, 77*(6), 1002-1016. doi: 10.1016/j.neuron.2013.03.007

Liu, Y. C., Cheng, J. K., & Lien, C. C. (2014). Rapid dynamic changes of dendritic inhibition in the dentate gyrus by presynaptic activity patterns. *J Neurosci, 34*(4), 1344-1357. doi: 10.1523/JNEUROSCI.2566-13.2014

Lobb, C. (2014). Abnormal Bursting as a Pathophysiological Mechanism in Parkinson's Disease. *Basal Ganglia, 3*(4), 187-195. doi: 10.1016/j.baga.2013.11.002

Lopez-Rojas, J., Heine, M., & Kreutz, M. R. (2016). Plasticity of intrinsic excitability in mature granule cells of the dentate gyrus. *Sci Rep, 6*, 21615. doi: 10.1038/srep21615

Lundstrom, B. N., & Fairhall, A. L. (2006). Decoding stimulus variance from a distributional neural code of interspike intervals. *J Neurosci, 26*(35), 9030-9037. doi: 10.1523/jneurosci.0225-06.2006

Madar, A. D., Ewell, L. A., & Jones, M. V. (2018). *Pattern separation of spiketrains in hippocampal neurons*. bioRxiv.

McKenzie, S., Frank, A. J., Kinsky, N. R., Porter, B., Riviere, P. D., & Eichenbaum, H. (2014). Hippocampal Representation of Related and Opposing Memories Develop within Distinct, Hierarchically Organized Neural Schemas. *Neuron, 83*(1), 202-215. doi: 10.1016/j.neuron.2014.05.019

McNaughton, B. L., & Morris, R. G. M. (1987). Hippocampal synaptic enhancement and information storage within a distributed memory system. *Trends in Neuroscience, 10*(10), 408-415.

Mease, R. A., Kuner, T., Fairhall, A. L., & Groh, A. (2017). Multiplexed Spike Coding and Adaptation in the Thalamus. *Cell Rep, 19*(6), 1130-1140. doi: 10.1016/j.celrep.2017.04.050

Mistry, R., Dennis, S., Frerking, M., & Mellor, J. R. (2011). Dentate gyrus granule cell firing patterns can induce mossy fiber long-term potentiation in vitro. *Hippocampus, 21*(11), 1157-1168. doi: 10.1002/hipo.20815

Mongiat, L. A., Esposito, M. S., Lombardi, G., & Schinder, A. F. (2009). Reliable activation of immature neurons in the adult hippocampus. *PLoS One, 4*(4), e5320. doi: 10.1371/journal.pone.0005320

Myers, C. E., & Scharfman, H. E. (2009). A role for hilar cells in pattern separation in the dentate gyrus: a computational approach. *Hippocampus, 19*(4), 321-337. doi: 10.1002/hipo.20516

Nakazawa, K. (2017). Dentate Mossy Cell and Pattern Separation. *Neuron, 93*(3), 465-467.

Neher, T., Cheng, S., & Wiskott, L. (2015). Memory storage fidelity in the hippocampal circuit: the role of subregions and input statistics. *PLoS Comput Biol, 11*(5), e1004250. doi: 10.1371/journal.pcbi.1004250

Neunuebel, J. P., & Knierim, J. J. (2014). CA3 retrieves coherent representations from degraded input: direct evidence for CA3 pattern completion and dentate gyrus pattern separation. *Neuron, 81*(2), 416-427. doi: 10.1016/j.neuron.2013.11.017

O'Keefe, J. (1976). Place units in the hippocampus of the freely moving rat. *Exp Neurol, 51*(1), 78-109.

O'Reilly, R. C., & McClelland, J. L. (1994). Hippocampal conjunctive encoding, storage, and recall: avoiding a trade-off. *Hippocampus, 4*(6), 661-682. doi: 10.1002/hipo.450040605

Oram, M., Wiener, M., Lestienne, R., & Richmond, B. (1999). Stochastic nature of precisely timed spike patterns in visual system neuronal responses. *J Neurophysiol, 81*(6), 3021-3033.

Osborne, L. C., Palmer, S. E., Lisberger, S. G., & Bialek, W. (2008). The neural basis for combinatorial coding in a cortical population response. *J Neurosci, 28*(50), 13522-13531. doi: 10.1523/jneurosci.4390-08.2008

Panzeri, S., Brunel, N., Logothetis, N. K., & Kayser, C. (2010). Sensory neural codes using multiplexed temporal scales. *Trends Neurosci, 33*(3), 111-120.

Pardi, M. B., Ogando, M. B., Schinder, A. F., & Marin-Burgin, A. (2015). Differential inhibition onto developing and mature granule cells generates high-frequency filters with variable gain. *Elife, 4*, e08764. doi: 10.7554/eLife.08764

Pernía-Andrade, Alejandro J., & Jonas, P. (2014). Theta-Gamma-Modulated Synaptic Currents in Hippocampal Granule Cells In Vivo Define a Mechanism for Network Oscillations. *Neuron, 81*(1), 140-152. doi: 10.1016/j.neuron.2013.09.046

Ramaswamy, S. (2015). Exciting times for inhibition: GABAergic synaptic transmission in dentate gyrus interneuron networks. *Front Neural Circuits, 9*, 13. doi: 10.3389/fncir.2015.00013

Ratté, S., Hong, S., De Schutter, E., & Prescott, S. A. (2013). Impact of neuronal properties on network coding: roles of spike initiation dynamics and robust synchrony transfer. *Neuron, 78*(5), 758-772.

Rieke, F., Warland, W., de Ruyter van Steveninck, R., & Bialek, W. (1999). *Spikes: Exploring the Neural Code*: THE MIT PRESS: A Bradford Book.

Robin, K., Maurice, N., Degos, B., Deniau, J. M., Martinerie, J., & Pezard, L. (2009). Assessment of bursting activity and interspike intervals variability: a case study for methodological comparison. *J Neurosci Methods, 179*(1), 142-149. doi: 10.1016/j.jneumeth.2009.01.020

Rolls, E. T. (2010). A computational theory of episodic memory formation in the hippocampus. *Behav Brain Res, 215*(2), 180-196. doi: 10.1016/j.bbr.2010.03.027

Santoro, A. (2013). Reassessing pattern separation in the dentate gyrus. *Front Behav Neurosci, 7*, 96. doi: 10.3389/fnbeh.2013.00096

Scharfman, H. E. (2016). The enigmatic mossy cell of the dentate gyrus. *Nat Rev Neurosci, 17*(9), 562-575. doi: 10.1038/nrn.2016.87

Scullin, C. S., & Partridge, L. D. (2012). Modulation by pregnenolone sulfate of filtering properties in the hippocampal trisynaptic circuit. *Hippocampus, 22*(11), 2184-2198. doi: 10.1002/hipo.22038

Senzai, Y., & Buzsáki, G. (2017). Physiological properties and behavioral correlates of hippocampal granule cells and mossy cells. *Neuron, 93*(3), 691-704. e695.

Temprana, S. G., Mongiat, L. A., Yang, S. M., Trinchero, M. F., Alvarez, D. D., Kropff, E., . . . Schinder, A. F. (2015). Delayed coupling to feedback inhibition during a critical period for the integration of adult-born granule cells. *Neuron, 85*(1), 116-130. doi: 10.1016/j.neuron.2014.11.023

Thorpe, S., Delorme, A., & Van Rullen, R. (2001). Spike-based strategies for rapid processing. *Neural Netw, 14*(6-7), 715-725.

Treves, A., Tashiro, A., Witter, M. P., & Moser, E. I. (2008). What is the mammalian dentate gyrus good for? *Neuroscience, 154*(4), 1155-1172. doi: 10.1016/j.neuroscience.2008.04.073

VanRullen, R., Guyonneau, R., & Thorpe, S. J. (2005). Spike times make sense. *Trends Neurosci, 28*(1), 1-4. doi: 10.1016/j.tins.2004.10.010

Weyand, T. G., Boudreaux, M., & Guido, W. (2001). Burst and tonic response modes in thalamic neurons during sleep and wakefulness. *J Neurophysiol, 85*(3), 1107-1118. doi: 10.1152/jn.2001.85.3.1107

Xie, X., Song, D., Wang, Z., Marmarelis, V. Z., & Berger, T. W. (2006). Interaction of short-term neuronal plasticity and synaptic plasticity revealed by nonlinear systems analysis in dentate granule cells. *Conf Proc IEEE Eng Med Biol Soc, 1*, 5543-5546. doi: 10.1109/iembs.2006.259706

Yim, M. Y., Hanuschkin, A., & Wolfart, J. (2014). Intrinsic rescaling of granule cells restores pattern separation ability of a dentate gyrus network model during epileptic hyperexcitability. *Hippocampus*. doi: 10.1002/hipo.22373

Yitzhaki, S. (2003). Gini's mean difference: A superior measure of variability for non-normal distributions. *Metron, 61*(2), 285-316.

Zylberberg, J., Hyde, R. A., & Strowbridge, B. W. (2016). Dynamics of robust pattern separability in the hippocampal dentate gyrus. *Hippocampus, 26*(5), 623-632. doi: 10.1002/hipo.22546

Supplements

This document provides supplementary figures, tables and a discussion on how to interpret the similarity and burstiness metrics used in the article "Temporal pattern separation in hippocampal neurons through multiplexed neural codes".

1 – How to interpret similarity metrics

Measuring the similarity between two spiketrains is a difficult problem (Cohen & Kohn, 2011; Cutts & Eglen, 2014), and many methods have been designed to this effect, each with a set of pros, cons and assumptions (Cutts & Eglen, 2014; Kreuz, 2011; Lyttle & Fellous, 2011; Rusu & Florian, 2014). To span a large range of potential neural codes, we used four different similarity metrics (R, NDP, SF, SPIKE) (Note: 'metrics' is used with a loose sense throughout the paper). Their pros, cons and assumptions are detailed in this section and summarized in **Table S1**.

Binned vs binless metrics

We used two different kinds of similarity metrics: 1) binned metrics (R, NDP, SF) consider a spiketrain as a list X of spike counts X_i (with X_i the number of spikes in time bin i of a given duration τ_w) and thus assume a neural code where spike counts are the basic informative feature; 2) a binless metric SPIKE that considers a spiketrain as a list of spike times and thus assumes a neural code where the spike times relative to the start of the given spiketrain are the basic informative feature.

Although R has already been used to measure the similarity between spiketrains (Cutts & Eglen, 2014; Yim et al., 2014), none of the binned metrics we used were designed with

spiketrains in mind and thus have properties that might not be well suited for the study of spiketrains. For instance, R, NDP and SF have the drawback of considering all X_i (i.e. binned spikecounts) as independent observations, which may not be a realistic assumption. Moreover, they assume spiketrains are related linearly, or that they belong to a Euclidean space. Binless metrics like SPIKE avoid these limitations (Aronov & Victor, 2004).

Differences between binned metrics

R vs NDP and SF: epistemological differences

The Pearson's correlation coefficient R was designed by early statisticians as a tool to quantify the strength and direction of a linear regression (Stanton, 2001). R thus considers two spiketrains X and Y as variables, with X_i and Y_i the observations, and assesses, across all i, whether X_i and Y_i tend to vary in a similar fashion (**Figure 2B**).

On the other hand, NDP and SF are metrics coming from the fields of Euclidean geometry and linear algebra. In contrast to R, they explicitly consider spiketrains as vectors, with each time bin i corresponding to a coordinate, or dimension, in an N-dimensional space (N being the total number of bins). NDP measures the angle between two vectors, and SF is based on vector norms (**Figure 2C**).

R, NDP and SF are not equivalent

Although they have been designed for different purposes, both R (Yim et al., 2014) and NDP (Aimone et al., 2009) have been used to measure the similarity between neuronal activity patterns (nb: NDP has never been used on spiketrains). In this context, NDP has sometimes

loosely been called a measure of correlation (Dieni et al., 2016). What difference is there between R and NDP then, especially in terms of the assumed neural code? A comparison of equation 1 and 2 (**Methods**) reveals that R is actually an NDP, but of baseline-subtracted vectors. In other words, R does not consider spiketrains as raw spikecount vectors but as vectors of deviation from their respective mean spikecount. This ensures that R is an optimal estimator of correlation (Stanton, 2001) but it has the inconvenience of not conserving the angular relationship between X and Y, making NDP necessary if one wants to evaluate pattern separation as an orthogonalization process. Moreover, using baseline-subtracted vectors also means that R considers common silent periods (i.e. $X_i = Y_i = 0$) as correlated, which is an assumption on the neural code that may be undesirable (Cutts & Eglen, 2014). In contrast, NDP excludes those empty bins and thus assumes a neural code where common periods of inactivity are irrelevant.

Comparing equations 1, 2 and 3 (**Methods**), the relationships between R, NDP and SF appear not trivial and not linear. To further evaluate the relationship between R, NDP and SF, we compared the values of each similarity metrics for all pairs of a set of simulated spiketrains. This set contained the $3^6 = 729$ possible spikecount vectors made of six bins, with each bin containing 0, 1 or 2 spikes (some examples are displayed in **Figure 2A**). This analysis confirmed that the three metrics are not equivalent and provides an intuition on what each metric represents (**Figure S1A**).

Interestingly, even though R, NDP and SF are not linearly related in principle, our measures of R and NDP between experimentally recorded spiketrains have a near linear relationship, as opposed to R and SF (**Figure S1B**). This correlation is likely due to our choice of input spiketrains as well as to biological constraints (e.g. refractory period) forcing the temporal structure of output spiketrains to vary only along certain dimensions. It is thus reflective of the

actual computations performed in the DG and shows that although R and NDP carry different sets of assumptions about the neural code, spiketrains recorded in GCs vary mostly along properties that both R and NDP are sensitive to.

R and NDP vs SF: sensitivity to individual firing rate differences and dependency on pairwise firing rate levels

To interpret R, NDP and SF and their different assumed neural codes, it is important to understand their relationship with the firing rate. Studying the impact of firing rate on similarity metrics can however mean different things.

First, a similarity metric can be sensitive to differences of firing rate between two spiketrains X and Y. For instance, if X = kY (with k an integer > 1), that means that X and Y have spikes in exactly the same bins (i.e. X and Y have the same temporal structure) but that Y has a higher firing rate. In such a case, both R and NDP would consider X and Y as perfectly similar (see example #2 in **Figure 2A-C**). In contrast, SF is designed to extract 1/k and thus strongly picks up on differences of firing rate. On the other hand, if X and Y have the same firing rate but that their spikes are in different bins (different temporal structure), R and NDP will consider those spiketrains completely dissimilar, and SF will see them as perfectly similar (see example #1 in **Figure 2A-C**). Other cases, where X and Y have spikes in the same time bins but only some bins have a different number of spikes (e.g. example #3 in **Figure 2A-C**) reveal that R and NDP are not totally insensitive to differences of firing rate when those are not proportional, but overall these two metrics are mostly sensitive to binwise synchrony, unlike SF (**Figure S2**).

Second, similarity metrics can be influenced by the overall firing rate level of a pair of spiketrain (for instance measured as the geometric mean of the firing rate of X and Y). Whether

an ideal similarity metric should be independent of the firing rate in such a way is debatable, and finding one is not trivial (Amari, 2009; Cutts & Eglen, 2014), yet it is generally seen as an undesirable property (Cutts & Eglen, 2014) because it makes the comparison of similarity values between two pairs of spiketrains more challenging to interpret (Cohen & Kohn, 2011). Indeed, for spiketrains X and Y with random spike times, the probability of spikes occurring close in time will intuitively be higher if X and Y have higher rates (de la Rocha et al., 2007), even though their temporal structure would be conserved.

Because R is often used to measure spiketrain correlations (Cohen & Kohn, 2011), its relationship to pairwise firing rate levels has already been studied. It was for instance demonstrated that, when X and Y are two Poisson spiketrains with the same rate λ, the normalization factor and the use of variables centered on their mean (which is, in the case of spiketrains, a linear function of the firing rate) makes R mathematically independent of λ (de la Rocha et al., 2007). However, in the general case, R has still a complex relationship with the firing rates of both spiketrains (Amari, 2009).

To get a better sense of this relationship for R, and study the effect of pairwise firing rate levels on NDP and SF as well, we considered two cases: 1) proportional firing rate increases, and 2) additive firing rate increases.

In the first case, we considered two spiketrains A and B such that $A = kX$ and $B = kY$ (with k an integer > 1). Some metrics aiming to measure the similarity between spiketrain in terms of temporal structure, like the correlation index, have been shown to result in higher values for the (A, B) pair compared to the (X, Y) pair (Cutts & Eglen, 2014). However, in this case, R, NDP and SF values would be the same for both pairs (A, B) and (X, Y): thanks to the

denominator in their respective formula, all three are insensitive to proportional increases in firing rates.

In the second case, we used the set of 729 6-bin spikecount vectors described above and generated new sets of related vectors with higher firing rates, such that for each spiketrain X of the original set there was a vector A in the new set with $A_i = X_i + k$ when $X_i > 0$, and $A_i = X_i$ otherwise. In other words, the rate was additively (not proportionally) increased while preserving the temporal structure of the initial spiketrains and maintaining constant the difference in the binwise number of spikes between spiketrains (e.g. for k = 5, if X = [010101] and Y = [020202], then A = [060606] and B = [070707]. For both pairs, the difference is [010101].). Our analysis shows that such an increase in the firing rate can affect all three metrics, but in different ways (**Figure S1C**): NDP and R can increase or decrease, and on average do not change much, whereas SF systematically increases. A larger increase of the firing rate leads to more variability of the effect size for NDP and R whereas the effect monotonically increases for SF.

SF is thus clearly dependent on pairwise firing rate levels, and R and NDP can be affected somewhat as well. Thus, to directly assess the variability of specific spiketrain features across a set of spiketrains (i.e. individual firing rate, compactness and occupancy) without contaminating interpretations with consideration of pairwise firing rate levels (especially in the case of SF), we used additional metrics detailed in **Methods – dispersion metrics**.

<u>Temporal resolution of binned metrics</u>

As binned metrics, R, NDP and SF are dependent on the binsize, i.e. a specified temporal resolution τ_w. In other words, in equations 1 to 3, X_i and Y_i are functions of τ_w. Temporal resolution logically influences the value of metrics measuring similarity in terms of the temporal

structure of spiketrains, such as R (Cohen & Kohn, 2011) or NDP. However it also influences SF: even though SF is sensitive to differences in firing rate, it is designed to be sensitive to differences in binwise firing rate, which makes it also sensitive to differences in burstiness even when the firing rate is constant (e.g. **Figure 4B** and **Figure S2**).

In **Figure 3**, we evaluated the influence of τ_w on our results by varying it between 5 ms and 1000 ms. Note that because our spiketrains are two-seconds long, using $\tau_w = 2000$ ms would mean the spiketrains can be seen as variables with only one observation, or as unidimensional vectors (i.e., scalars) that can only vary by their norm (i.e., firing rate). In this case, R is meaningless, NDP is necessarily 1, which indicates collinearity and SF would directly assess the difference in total spike number (i.e. overall firing rate) between the two spiketrains.

Table S1. Assumptions on the neural code assumed by four similarity metrics

	R	**NDP**	**SF**	**SPIKE**
Binned (spike count code)	X	X	X	
Binless (spike time code)				X
Preserved time relationship between time points or bins				X
"raw" spikecount vectors		X	X	
Assumption of linear relationship between spiketrains	X	X	X	
Assumption of Euclidean space	X	X	X	
Excludes common periods of silence		X		
Mostly sensitive to binwise synchrony	X	X		
Sensitive to spike time synchrony				X
Sensitive to differences in firing rate or burstiness between spiketrains			X	X

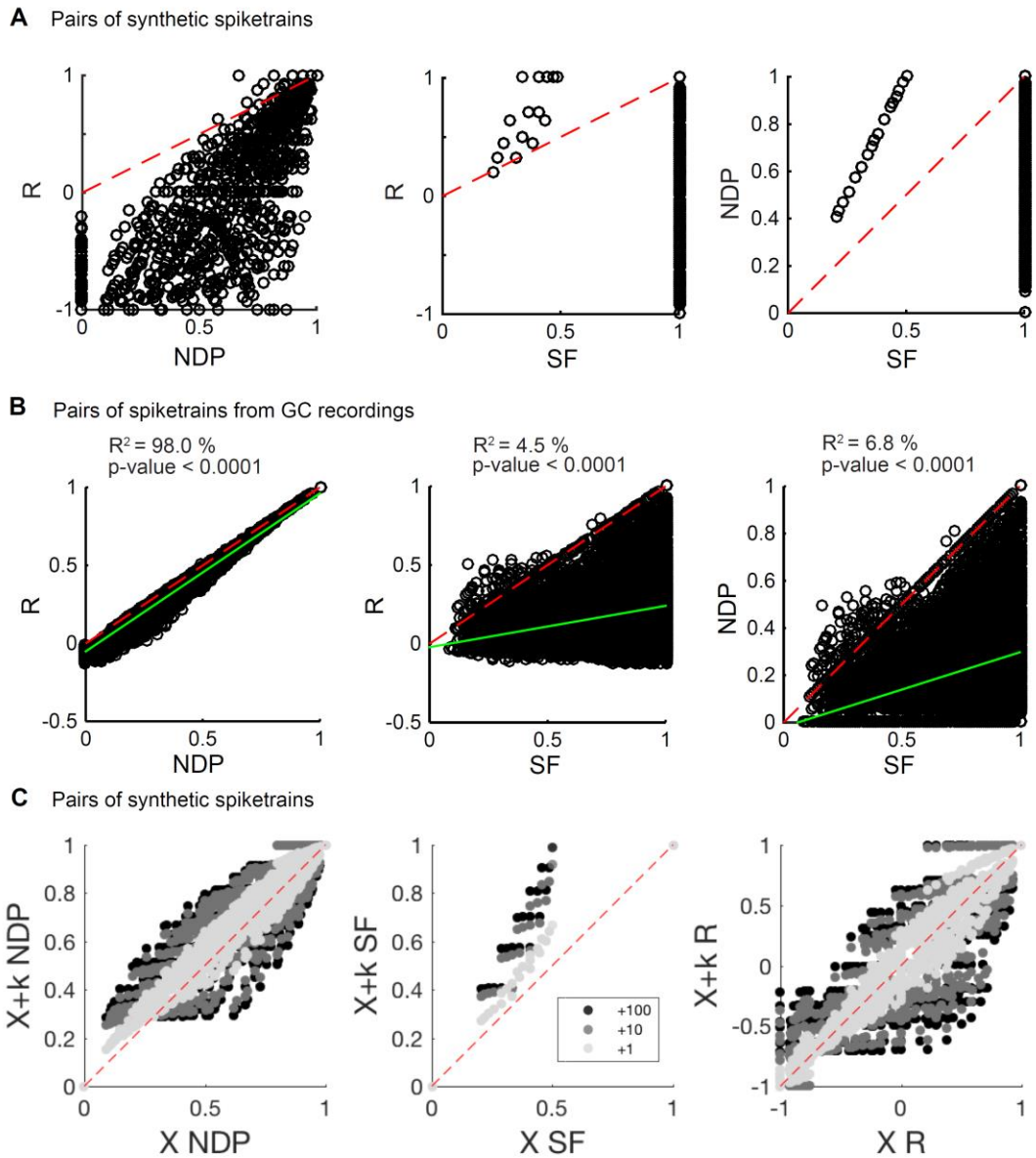

Figure S1 (related to Figure 2). **R, NDP and SF are not equivalent.**
(A) Relationships between these 3 similarity metrics (R, NDP and SF) computed between the 3^6 possible spikecount vectors with six bins and that can have 0, 1 or 2 spikes per bin (All pairs combinations = 499,500 data points).
(B) Relationships between these three similarity metrics for the 124,950 pairs of spiketrains from the 102 experimental GC recording sets. Green lines correspond to a linear regression (R^2 and p-value in each panel). Note that although R and NDP are well correlated in our experimental data (R^2>0.95), there is not a linear relationship between R and NDP in theory.
(**C**) Impact of non-proportional firing rate increase on similarity values for all three metrics. For each 6-bin spikecount vector X (same as in A), a vector A was generated such that for each bin i with at least one spike, $A_i = X_i + k$, with k = 1, 10 or 100, and $A_i = X_i$ when $X_i = 0$ (e.g. for k = 1, if X = [010101] and Y = [020202], then A = [020202] and B = [030303]. For both pairs, the difference is [010101]). NDP, SF and R values were computed for all pairs in each set of vectors, and the values of the initial set (x-axis) was compared to the values of the X+k set (y-axis). Data points away from the identity line (red) demonstrate an effect of the firing rate increase.

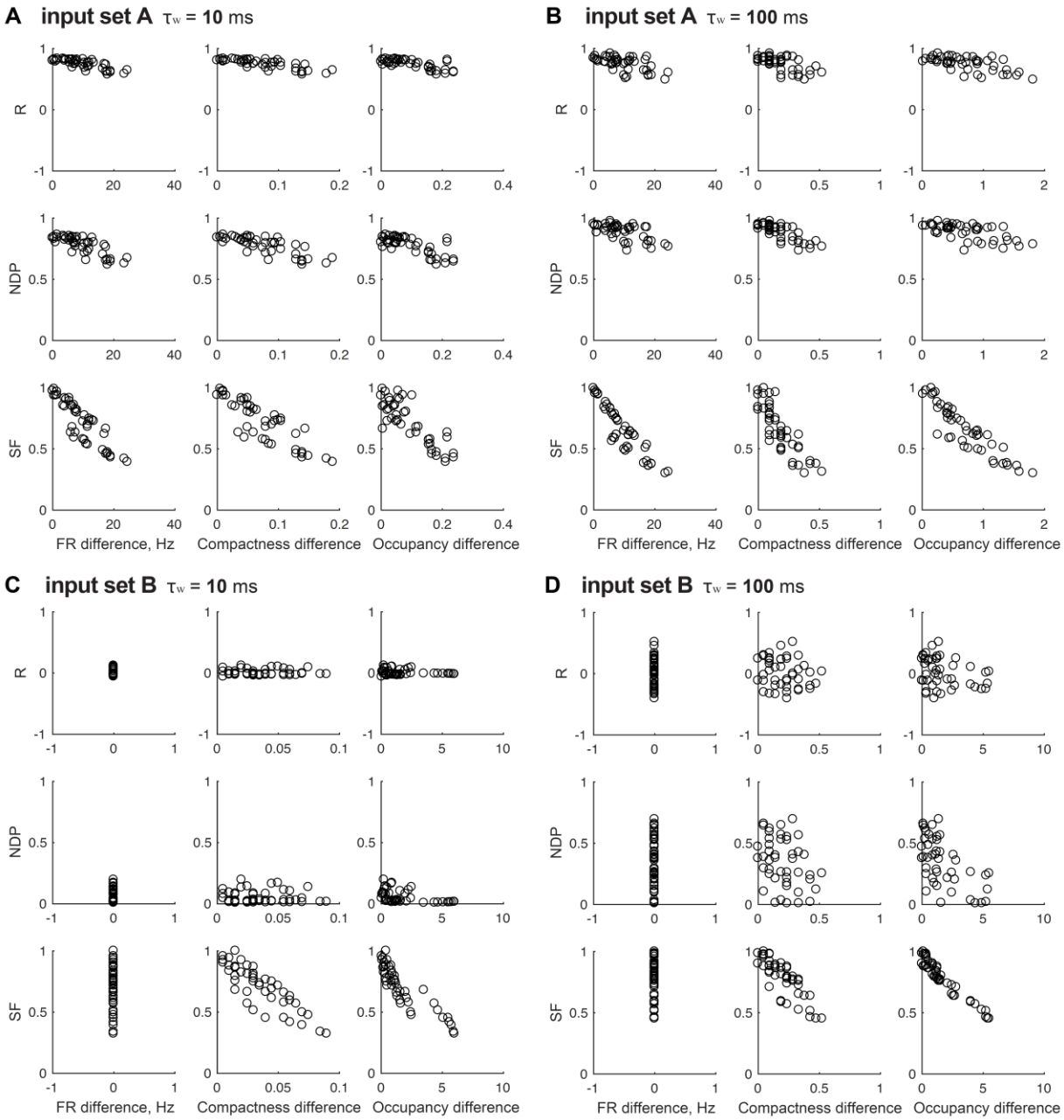

Figure S2 (related to Figure 4)**. Influence of firing rate and burstiness differences on binned similarity metrics.**

Data points correspond to single pairs of input trains from input set A (**A-B**) or input set B (**C-D**). The similarity between two spiketrains (R, NDP or SF), their difference of compactness (proportion of occupied bins), and their difference in occupancy (average number of spikes per occupied bins) were measured using binning windows of 10 ms (**A, C**) or 100 ms (**B, D**). When FR is constant across spiketrains, compactness and occupancy differences are direct measures of burstiness differences, given a certain timescale. As intuited from Figure 2A-C, SF is very sensitive to variations in FR, compactness and occupancy between spiketrains, whereas R and NDP are only mildly influenced at best (and mostly at larger timescales), by such variations.

2 – Burstiness metrics

Cell burstiness vs spiketrain burstiness

To assess the tendency of a neuron to fire bursts, we computed the Kullback-Liebler divergence $D_{KL}(M||P)$ of the ISI distribution in a set of output spiketrains from the ISI distribution of a Poisson process. $D_{KL}(M||P)$ is an asymmetric, information theory-based measure of the inefficiency of the assumption that the distribution of ISI M is a distribution P (Poisson, in our case), and thus can be interpreted as the divergence of one probability distribution from another. Note that a train with regularly spaced spikes would diverge from Poissonness without being bursty, but that natural spiketrains are rarely regular, and accordingly none of our recordings showed a regular ISI distribution, suggesting that $D_{KL}(M||P)$ is a good indirect indicator of burstiness.

The D_{KL} approach above has the advantage of being independent of the firing rate, but has two limitations. First it is parametric, based on the nonconsensual opinion that a Poisson process is the least bursty of processes (Gourevitch & Eggermont, 2007). Second, because it is based on the comparison of ISI distributions, it requires a large sample of ISIs to be accurate and thus cannot be used to measure the burstiness of a single two second spiketrain.

In order to assess the burstiness of single spiketrains, we designed two binned metrics: compactness and occupancy. We used binned metrics to avoid the difficult problem of burst detection that generally requires some arbitrary threshold to define what is considered a burst (Cotterill et al., 2016). Unlike D_{KL} these metrics are not independent of the firing rate, but together they allow distinguishing between burstiness and firing rate (see below).

Compactness and occupancy: complementary relationships to the firing rate allow disambiguating between burstiness and lack of sparseness

It is unclear whether the concept of burstiness should be independent or not of the firing rate (for instance, should we consider a spiketrain with 100 spikes clustered in the same 10 ms bin as bursty as a spiketrain with just 10 spikes in a single bin?), but, as explained above for similarity metrics, a dependency of burstiness metrics on the firing rate can make interpretations more challenging. Both compactness and occupancy are dependent on the firing rate, but in different ways, which resolves the ambiguity: 1) Compactness doesn't provide information on the firing rate per se, and is only related to the firing rate in the sense that, in the case of Poisson-like spiking, higher rates lead to a higher chance of occupying a large number of bins. Thus a spiketrain with just one spike will be considered as compact as a spiketrain with a large number of spikes all clustered into one bin. In contrast, the occupancy is directly related to the number of spikes and thus to the firing rate of a given spiketrain (Indeed, when considering a time bin as long as the full duration of a spiketrain, i.e. two seconds in our case, the occupancy is exactly proportional to the firing rate.). Occupancy would thus distinguish between a sparse spiketrain with just one spike (Occupancy = 1) and a spiketrain with 10 spikes clustered in one bin (Occupancy = 10). 2) On the other hand, spiketrains with different firing rates can have the same occupancy (e.g. if all spikes are distributed in different bins, Occupancy = 1 regardless of the number of spikes) but would be differentiated by their level of compactness (100 distributed spikes would be considered much less compact than a spiketrain with just one spike). Therefore, when assessing pairs of spiketrains with different firing rates, compactness and occupancy provide complementary information that allows determining whether one spiketrain is unambiguously burstier or simply has a higher firing rate (see **Table S2**).

Table S2. (related to Figure 7) **How to interpret compactness and occupancy in terms of burstiness and sparseness when comparing two spiketrains?**

The table shows what it means when *compactness* (C) is increased, stays constant or decreases while *occupancy* (O) increases, stays constant or decreases. We distinguish the cases when the mean firing rate (FR) is constant (FR absolute difference = 0) or different (FR abs diff > 0). The second spiketrain is either unambiguously burstier (B+) or less bursty (B-), has a greater FR (F+) or is sparser (F-), or a combination of those (i.e. B+F+ or B-F-). In each case, we provide an example (4-dimensional vectors of spike counts) when the conditions can coexist (NA means not applicable). Notice that the resulting table of examples is centrally symmetric.

C \ O		↗	–	↘
↗	FR abs diff = 0	**B+** 0101 → 0200	NA	NA
	FR abs diff > 0	**B+F+** 0111 → 0501	**F-** 0202 → 0200	**F-** 0222 → 0101
–	FR abs diff = 0	NA	2020 → 0202	NA
	FR abs diff > 0	**F+** 0101 → 0202	NA	**F-** 0202 → 0101
↘	FR abs diff = 0	NA	NA	**F-** 0200 → 0101
	FR abs diff > 0	**F+** 0101 → 0222	**F+** 0200 → 0202	**B-F-** 0501 → 0111

References

Aimone, J. B., Wiles, J., & Gage, F. H. (2009). Computational influence of adult neurogenesis on memory encoding. *Neuron, 61*(2), 187-202. doi: 10.1016/j.neuron.2008.11.026

Amari, S.-i. (2009). Measure of correlation orthogonal to change in firing rate. *Neural Comput, 21*(4), 960-972.

Aronov, D., & Victor, J. D. (2004). Non-Euclidean properties of spike train metric spaces. *Physical Review E, 69*(6), 061905.

Cohen, M. R., & Kohn, A. (2011). Measuring and interpreting neuronal correlations. *Nat Neurosci, 14*(7), 811.

Cotterill, E., Charlesworth, P., Thomas, C. W., Paulsen, O., & Eglen, S. J. (2016). A comparison of computational methods for detecting bursts in neuronal spike trains and their application to human stem cell-derived neuronal networks. *J Neurophysiol, 116*(2), 306-321. doi: 10.1152/jn.00093.2016

Cutts, C. S., & Eglen, S. J. (2014). Detecting pairwise correlations in spike trains: an objective comparison of methods and application to the study of retinal waves. *J Neurosci, 34*(43), 14288-14303. doi: 10.1523/jneurosci.2767-14.2014

de la Rocha, J., Doiron, B., Shea-Brown, E., Josic, K., & Reyes, A. (2007). Correlation between neural spike trains increases with firing rate. *Nature, 448*(7155), 802-806. doi: 10.1038/nature06028

Dieni, C. V., Panichi, R., Aimone, J. B., Kuo, C. T., Wadiche, J. I., & Overstreet-Wadiche, L. (2016). Low excitatory innervation balances high intrinsic excitability of immature dentate neurons. *Nat Commun, 7*, 11313. doi: 10.1038/ncomms11313

Gourevitch, B., & Eggermont, J. J. (2007). A nonparametric approach for detection of bursts in spike trains. *J Neurosci Methods, 160*(2), 349-358. doi: 10.1016/j.jneumeth.2006.09.024

Kreuz, T. (2011). Measures of spike train synchrony. *Scholarpedia, 6*(10). Retrieved from Scholarpedia website: http://www.scholarpedia.org/article/Measures_of_spike_train_synchrony doi:10.4249

Lyttle, D., & Fellous, J. M. (2011). A new similarity measure for spike trains: sensitivity to bursts and periods of inhibition. *J Neurosci Methods, 199*(2), 296-309. doi: 10.1016/j.jneumeth.2011.05.005

Rusu, C. V., & Florian, R. V. (2014). A new class of metrics for spike trains. *Neural Comput, 26*(2), 306-348.

Stanton, J. M. (2001). Galton, Pearson, and the peas: A brief history of linear regression for statistics instructors. *Journal of Statistics Education, 9*(3).

Yim, M. Y., Hanuschkin, A., & Wolfart, J. (2014). Intrinsic rescaling of granule cells restores pattern separation ability of a dentate gyrus network model during epileptic hyperexcitability. *Hippocampus*. doi: 10.1002/hipo.22373